Neurobiology of Disease

Impairment of the Glial Phagolysosomal System Drives Prion-Like Propagation in a *Drosophila* Model of Huntington's Disease

Graham H. Davis,[1,2,3] Aprem Zaya,[3] and Margaret M. Panning Pearce[1,2,3]

[1]Department of Biological and Biomedical Sciences, Rowan University, Glassboro, New Jersey 08028, [2]Department of Biology, Saint Joseph's University, Philadelphia, Pennsylvania 19131, and [3]Department of Biological Sciences, University of the Sciences, Philadelphia, Pennsylvania 19104

Protein misfolding, aggregation, and spread through the brain are primary drivers of neurodegenerative disease pathogenesis. Phagocytic glia are responsible for regulating the load of pathological proteins in the brain, but emerging evidence suggests that glia may also act as vectors for aggregate spread. Accumulation of protein aggregates could compromise the ability of glia to eliminate toxic materials from the brain by disrupting efficient degradation in the phagolysosomal system. A better understanding of phagocytic glial cell deficiencies in the disease state could help to identify novel therapeutic targets for multiple neurological disorders. Here, we report that mutant huntingtin (mHTT) aggregates impair glial responsiveness to injury and capacity to degrade neuronal debris in male and female adult *Drosophila* expressing the gene that causes Huntington's disease (HD). mHTT aggregate formation in neurons impairs engulfment and clearance of injured axons and causes accumulation of phagolysosomes in glia. Neuronal mHTT expression induces upregulation of key innate immunity and phagocytic genes, some of which were found to regulate mHTT aggregate burden in the brain. A forward genetic screen revealed Rab10 as a novel component of Draper-dependent phagocytosis that regulates mHTT aggregate transmission from neurons to glia. These data suggest that glial phagocytic defects enable engulfed mHTT aggregates to evade lysosomal degradation and acquire prion-like characteristics. Together, our findings uncover new mechanisms that enhance our understanding of the beneficial and harmful effects of phagocytic glia in HD and other neurodegenerative diseases.

Key words: **aggregate; glia; huntingtin; phagocytosis; prion-like; Rab**

Significance Statement

Deposition of amyloid aggregates is strongly associated with neurodegenerative disease progression and neuronal cell loss. Many studies point to glial cells as dynamic mediators of disease, capable of phagocytosing toxic materials, but also promoting chronic inflammation and proteopathic aggregate spread. Thus, glia have emerged as promising therapeutic targets for disease intervention. Here, we demonstrate in a *Drosophila* model of Huntington's disease that neuronal mHTT aggregates interfere with glial phagocytic engulfment, phagolysosomal processing, and innate immunity transcriptional responses. We also identify Rab10 as a novel modifier of prion-like transmission of mHTT aggregates. Our findings add to a growing narrative of glia as double-edged players in neurodegenerative diseases.

Received July 6, 2023; revised Jan. 31, 2024; accepted Feb. 26, 2024.

Author contributions: G.H.D., A.Z., and M.M.P.P. designed research; G.H.D. and A.Z. performed research; M.M.P.P. contributed unpublished reagents/analytic tools; G.H.D., A.Z., and M.M.P.P. analyzed data; G.H.D. and M.M.P.P. wrote the paper.

We would like to thank Sabrina Abbruzzese, Ryan Buist, Georgiana Moore, and David Tomlinson for experimental assistance, and all former and current members of the Pearce Lab for their support and many fruitful discussions about this project. This work was supported by funding from University of the Sciences, Rowan University, the W.W. Smith Charitable Trusts, and the National Institutes of Health (awards NS128847, AG063295, and 1S10OD032124).

The authors declare no competing financial interests.

Correspondence should be addressed to Margaret M. Panning Pearce at pearcem@rowan.edu.

https://doi.org/10.1523/JNEUROSCI.1256-23.2024

Introduction

Neuron-glia crosstalk is critical for maintaining homeostasis in the central nervous system (CNS), and disruption of these intercellular interactions is increasingly recognized as a central component of many neurological disorders, including neurodegenerative diseases. Glia perform immune surveillance functions in the CNS and respond to neuronal injury by altering gene expression (Magaki et al., 2018) and clearing damaged cells (Raiders et al., 2021; Zheng and Tuszynski, 2023). These glial responses may initially be neuroprotective, but prolonged glial reactivity propels the neurodegenerative disease state, for

example, by driving premature loss of living neurons or functional synapses (Neniskyte et al., 2011; Hong et al., 2016; Dejanovic et al., 2022) and inducing neuroinflammation (Liddelow et al., 2017). Expanding our understanding of how glia influence neuron function and survival could reveal promising new therapeutic strategies for neurodegenerative diseases.

A pathological hallmark of most neurodegenerative diseases is the accumulation of misfolded proteins into intra- or extracellular amyloid aggregates in vulnerable regions of the CNS (Knowles et al., 2014). Protein aggregates form due to age-associated decline in cellular protein folding capacity (Santra et al., 2019; Stein et al., 2022) and overwhelming of degradative pathways, including the ubiquitin–proteasome system, autophagy, and phagocytosis (Aman et al., 2021; Duong et al., 2021; Wodrich et al., 2022). As professional phagocytes of the brain, microglia and astrocytes clear damaged and dysfunctional cells (Paolicelli et al., 2011; Wakida et al., 2018; Herzog et al., 2019; J-H. Lee et al., 2021) and other pathogenic material, such as protein aggregates (C-C. Liu et al., 2017; Choi et al., 2020). Defective glial clearance of debris may be a driving force underlying neurodegenerative disease, highlighted by a growing list of genetic risk variants associated with phagocytic and endolysosomal pathways (Podleśny-Drabiniok et al., 2020). Endolysosomal impairment promotes protein aggregate accumulation; in turn, aggregates can drive further endolysosomal dysfunction, including deacidification and membrane permeabilization of intracellular vesicles (Krasemann et al., 2017; Heckmann et al., 2019; Burbidge et al., 2022; J-H. Lee et al., 2022). Aggregates that escape degradation may gain the ability to spread and seed soluble proteins in a prion-like manner (Jucker and Walker, 2018; Monaco and Fraldi, 2020).

Mechanisms by which pathogenic aggregates dysregulate endolysosomal processing remain largely unknown. Intracellular membrane fusion events that regulate endo/phagosome maturation are catalyzed by Rab GTPases (Ng and Tang, 2008; Chan et al., 2011; Langemeyer et al., 2018), enzymes that cycle between active (GTP-bound) and inactive (GDP-bound) states to organize endomembranes into distinct functional domains (Hall, 1990; Chan et al., 2011). Rab dysfunction is implicated in several neurodegenerative diseases—e.g., upregulation of Rab4, Rab5, Rab7, and Rab27 has been observed in Alzheimer's disease (AD) (Ginsberg et al., 2011), and several Rabs are known substrates of leucine-rich repeat kinase 2 (LRRK2), a genetic risk factor in familial Parkinson's disease (PD) (Jeong et al., 2018). Intriguingly, spread of α-synuclein between cultured neuronal and enteroendocrine cells is mediated by the LRRK2 substrate Rab35 (Bae et al., 2018; Rodrigues et al., 2022), suggesting that Rab-dependent processes may contribute to formation and propagation of prion-like aggregate seeds.

Here, we investigated the impact of protein aggregates generated in neurons on phagocytic glial cell functions in a *Drosophila* model of Huntington's disease (HD). We reported that neuronal expression of aggregation-prone mutant huntingtin (mHTT) protein reduces the ability of glia to clear axonal debris and to mount phagocytic and innate immunity transcriptional responses following acute nerve injury. We also observed mHTT-induced changes to numbers of glial lysosomes and Rab+ vesicles in uninjured brains and identified Rab10 as a novel modifier of prion-like spreading of mHTT aggregates in adult fly brains. Together, these studies shed light on mechanisms by which phagocytic glia respond to and are impaired by accumulation of pathogenic aggregates in neurons.

Materials and Methods

Fly husbandry. Fly stocks and crosses were raised on standard cornmeal/molasses media on a 12 h light/12 h dark cycle at 25°C, unless otherwise noted. No sex-specific differences were observed in any experiments, so both males and females were utilized in this study. Transgenic or mutant flies were either generated for this study (described below), purchased from Bloomington Drosophila Stock Center, or kindly provided by collaborators. Genotypes and sources of all fly stocks used in this study are listed in Table 1, and complete genotypes of flies used in each figure are listed in Table 2.

Acute antennal nerve injury was performed by bilateral removal of the second and third antennal segments from anesthetized adult flies (MacDonald et al., 2006). For quantitative PCR analyses, maxillary palps were removed in addition to third antennal segments to sever all olfactory receptor neuron (ORN) axons. Axotomized flies were incubated for the indicated times on standard media prior to dissection and processing for imaging.

Cloning and Drosophila *transgenesis.* pUASTattB(HTT_{ex1}Q25-V5) and pUASTattB(HTT_{ex1}Q91-V5) plasmids were cloned by PCR amplification of HTT exon 1 (HTT_{ex1}) cDNA using a reverse primer that inserted an in-frame, C-terminal V5 epitope tag (GKPIPNPLLGLDST) and ligation into the pQUASTattB vector backbone via XhoI and XbaI restriction sites. pQUASTattB(HTT_{ex1}Q25-GFP) and pQUASTattB(HTT_{ex1}Q91-GFP) were generated by replacing the mCherry sequence in pQUASTattB(HTT_{ex1}Q25-mCherry) and pQUASTattB(HTT_{ex1}Q91-mCherry) plasmids previously generated by our lab (Pearce et al., 2015) with an in-frame, C-terminal GFP sequence via Gibson Assembly (New England Biolabs, Inc.). pUASTattB(pHluorin-HTT_{ex1}Q25-tdTomato) and pUASTattB(pHluorin-HTT_{ex1}Q91-tdTomato) plasmids were generated by PCR amplification of HTT_{ex1} cDNAs and subcloning to replace the CD4 sequence in the pUASTattB(MApHS) plasmid (Han et al., 2014) via In-Fusion cloning (Takara Bio USA, Inc.). pUASTattB(mCherry-Galectin-3) and pUASTattB(mCherry-Galectin-8) were cloned by PCR amplification of human LGals3 and LGals8 cDNAs from the pHAGE-mKeima-LGALS3 and pHAGE-FLAG-APEX2-LGALS8 plasmids (Addgene plasmids #175780 and #175758) (Eapen et al., 2021) and insertion downstream of an in-frame mCherry sequence in the pUASTattB vector backbone via Gibson Assembly.

Plasmids were microinjected into *w-* embryos with the su(Hw)attP8, attP24, VK19, or VK27 ϕC31 attP integration sites at BestGene, Inc. Table 1 lists detailed genotype information for all transgenic flies generated in this study.

Drosophila brain dissection and sample preparation. Adult fly brains were dissected in ice-cold phosphate-buffered saline (PBS) containing no detergent or 0.03% (PBS/0.03T), 0.1% (PBS/0.1T), or 0.3% (PBS/0.3T) Triton X-100. Dissected brains were fixed in 4% paraformaldehyde (PFA) in the dark at room temperature (RT) for 20 min. For imaging of GFP or mCherry fluorescence signals, brains were washed 7× in PBS/0.03T buffer before incubation in Slowfade Gold Antifade Mountant (Invitrogen). When imaging pHluorin-tagged and other pH-sensitive constructs, such as GFP-LAMP1, brains were washed 7× in PBS for at least 50 min at RT before incubation in Slowfade. For immunostaining, brains were washed 7× in PBS/0.3T after fixation, blocked in PBS/0.3T containing 5% normal goat serum (Lampire Biological Laboratories) for 30 min at RT, incubated in primary antibodies diluted in blocking solution for 24–48 h at 4°C, washed 7× in PBS/0.3T, and then incubated in secondary antibodies diluted in blocking solution for 16–20 h at 4°C. After a final set of 7× PBS/0.3T washes, dissected brains were incubated in Slowfade. For Magic Red and LysoTracker staining, brains were dissected in PBS and incubated in 1:1,000 LysoTracker Red DND-99 (Invitrogen) or 1:1,250 Magic Red (ImmunoChemistry) diluted in PBS for 20 min at RT. Brains were washed 5× in PBS for 15 min total, fixed in 4% PFA in PBS/0.1T for 20 min at RT, washed 6× in PBS/0.1T for 30 min total, and incubated in Slowfade. Following incubation in Slowfade for 1–24 h at 4°C in the dark, all brains were bridge-mounted in Slowfade on glass microscopy slides under #1.5 cover glass, and edges were sealed using clear nail polish.

Table 1. *Drosophila* genotype and source information

Name	ID (if available)	Reference	Notes
Or67d-QF		Liang et al., 2013	
repo-Gal4	RRID:BDSC_7415	Sepp et al., 2001	
mz0709-Gal4		Ito et al., 1995	A gift from Marc Freeman (Vollum Institute)
alrm-Gal4	RRID:BDSC_67032		
orco-Gal4	RRID:BDSC_23292		
Or47b-Gal4	RRID:BDSC_9983		
QUAS-HTT$_{ex1}$Q25-mCherry^{attP24}		Donnelly et al., 2020	
QUAS-HTT$_{ex1}$Q91-mCherry^{attP24}		Donnelly et al., 2020	
QUAS-HTT$_{ex1}$Q91-mCherry^{attP3}		Donnelly et al., 2020	
QUAS-HTT$_{ex1}$Q91-mCherry$^{suHw(attP8)}$		This study	
UAS-HTT$_{ex1}$Q25-GFP		Donnelly et al., 2020	
UAS-HTT$_{ex1}$Q91-GFP		Donnelly et al., 2020	
UAS-GFP		Donnelly et al., 2020	
QUAS-HTT$_{ex1}$Q25-GFP		This study	
QUAS-HTT$_{ex1}$Q91-GFP		This study	
UAS-mCherry-LGals3		This study	
UAS-mCherry-LGals8		This study	
QUAS-HTT$_{ex1}$Q25-V5		This study	
QUAS-HTT$_{ex1}$Q91-V5		This study	
UAS-pHluorin-HTT$_{ex1}$Q25-tdTomato		This study	
UAS-pHluorin-HTT$_{ex1}$Q91-tdTomato		This study	
UAS-mCD8-GFP	RRID:BDSC_5137		
UAS-Draper^{RNAi}		Logan et al., 2012	A gift from Marc Freeman (Vollum Institute)
tubP-Gal80^{ts}	RRID:BDSC_7017		
UAS-Drs^{RNAi}	RRID:BDSC_55391		
UAS-PGRP-SA^{RNAi}	RRID:BDSC_60037		
UAS-MMP1^{RNAi}	RRID:BDSC_31489		
UAS-ets21c^{RNAi}	RRID:BDSC_39069		
UAS-mCherry^{RNAi}	RRID:BDSC_35785		
UAS-rel^{RNAi}	RRID:BDSC_33661, RRID BDSC_28943		
UAS-dl^{RNAi}	RRID:BDSC_38905, RRID:BDSC_32934, RRID:BDSC_34938, RRID: BDSC_27650, RRID:BDSC_36650		
UAS-NinjurinA^{RNAi}	RRID:BDSC_50632, RRID:BDSC_51358		
UAS-Toll-6^{RNAi}	RRID:BDSC_56048, RRID:BDSC_64968		
Orco-QF2	RRID:BDSC_91997		
Tl{Tl}Rab10^{YFP}	RRID:BDSC_62548		
Tl{Tl}Rab5^{YFP}	RRID:BDSC_62543		
Tl{Tl}Rab7^{YFP}	RRID:BDSC_62545		
UAS-MApHS		Han et al., 2014	A gift from Chun Han (Cornell University)
Repo-Cas9[6A]		Koreman et al., 2021	A gift from Chun Han (Cornell University)
gRNA-drpr(BR)		Sapar et al., 2018	A gift from Chun Han (Cornell University)
Jra-GFP.FLAG	RRID:BDSC_50755		
OK107-Gal4			
UAS-GFP-LAMP1		Pulipparacharuvil et al., 2005	A gift from Helmut Kramer (UT Southwestern)
UAS-LAMP1-GFP	RRID:BDSC_42714		*nSyb-Gal4* was removed from stock
UAS-Rbcn-3a^{RNAi}	RRID:BDSC_34612		
UAS-Spinster^{RNAi}	RRID:BDSC_27702		
UAS-Vha100-2^{RNAi}	RRID:BDSC_64859		
UAS-Vha16-1^{RNAi}	RRID:BDSC_40923		
UAS-Vha68-3^{RNAi}	RRID:BDSC_42954		
UAS-YFP-Rab5	RRID:BDSC_9775		
UAS-YFP-Rab7	RRID:BDSC_23641		
UAS-YFP-Rab10	RRID:BDSC_24097		
UAS-YFP-Rab10 (T23N)	RRID:BDSC_9788		
UAS-YFP-Rab10 (Q68L)	RRID:BDSC_23259		
UAS-Rab7^{RNAi}	RRID:BDSC_27051		
UAS-Rab10^{RNAi}	RRID:BDSC_26289		
UAS-Rab2^{RNAi}	RRID:BDSC_28701, RRID:BDSC_34922		
UAS-Rab6^{RNAi}	RRID:BDSC_27490, RRID:BDSC_35744		
UAS-Rab11^{RNAi}	RRID:BDSC_27730		
UAS-Rab3^{RNAi}	RRID:BDSC_34655		
UAS-Rab14^{RNAi}	RRID:BDSC_28708		
UAS-Rab4^{RNAi}	RRID:BDSC_33757		
UAS-Rab5^{RNAi}	RRID:BDSC_30518		

(*Table continues.*)

Table 1. Continued

Name	ID (if available)	Reference	Notes
UAS-Rab8^{RNAi}	RRID:BDSC_27519, RRID:BDSC_34373		
UAS-Rab9^{RNAi}	RRID:BDSC_42942, RRID:BDSC_34374		
UAS-luciferase^{RNAi}	RRID:BDSC_31603		
UAS-Rab9Db^{RNAi}	RRID:BDSC_38269		
UAS-Rab32^{RNAi}	RRID:BDSC_38956, RRID:BDSC_28002		
UAS-Rab18^{RNAi}	RRID:BDSC_34734, RRID:BDSC_27665		
UAS-RabX4^{RNAi}	RRID:BDSC_44070		
UAS-Rab27^{RNAi}	RRID:BDSC_50537		
UAS-RabX2^{RNAi}	RRID:BDSC_53928		
UAS-Rab39^{RNAi}	RRID:BDSC_53995		
UAS-Rab23^{RNAi}	RRID:BDSC_55352, RRID:BDSC_63689, RRID:BDSC_36091, RRID:BDSC_28025		
UAS-Rab35^{RNAi}	RRID:BDSC_67952, RRID:BDSC_80457		
UAS-Rab40^{RNAi}	RRID:BDSC_80472		
UAS-RabX6^{RNAi}	RRID:BDSC_26281, RRID:BDSC_53252		
UAS-Rab19^{RNAi}	RRID:BDSC_34607		
UAS-Rab21^{RNAi}	RRID:BDSC_29403		
UAS-Rab27^{RNAi}	RRID:BDSC_35774		
UAS-Draper-I		Logan et al., 2012	A gift from Marc Freeman (Vollum Institute)
Rab10(CRISPR-KO)		Kohrs et al., 2021	A gift from P. Robin Heisinger (Freie Universität Berlin)

Primary antibodies used in this study include: chicken anti-GFP (RRID: AB_300798; 1:1,000; Abcam), chicken anti-GFP (RRID: AB_2534023; 1:500; Thermo Fisher Scientific Inc.), rat anti-N-cadherin (clone DN-Ex #8; RRID: AB_528121; 1:75; Developmental Studies Hybridoma Bank), mouse anti-Repo (clone 8D12; RRID: AB_528448; 1:25; Developmental Studies Hybridoma Bank), mouse anti-V5 (RRID: AB_2556564; 1:125; Thermo Fisher Scientific Inc.), and rabbit anti-Draper (1:500; a kind gift from Marc Freeman, Vollum Institute). Secondary antibodies include: AlexaFluor 405 goat anti-rabbit (RRID: AB_221605; 1:250), FITC-conjugated donkey anti-chicken (RRID: AB_2340356; 1:250; Jackson Immuno Research Labs), AlexaFluor 568 goat anti-mouse (RRID: AB_2534072; 1:250), AlexaFluor 647 goat anti-rabbit (RRID: AB_2535812; 1:250), and AlexaFluor 647 goat anti-rat IgGs (RRID: AB_141778; 1:250) (Invitrogen).

Image acquisition. All microscopy data were collected on a Leica SP8 laser-scanning confocal system equipped with 405, 488, 561, and 633 nm lasers and 40× 1.3 NA or 63× 1.4 NA oil objective lenses. Leica LAS-X software was used to establish optimal settings during each microscopy session and to collect optical *z*-slices of whole-mounted brain samples with Nyquist-optimized sampling criteria. Optical zoom was used to magnify and establish a region of interest (ROI) in each sample. For images showing a single glomerulus, confocal slices were collected to generate ∼73 × 73 × 20 µm (*xyz*) stacks, with *z*-axis boundaries established using fluorescent signal in DA1 or VA1lm ORN axons. For images of a single antennal lobe, confocal slices were collected to generate ∼117 × 117 × 26 µm (*xyz*) stacks, which were located using HTT_{ex1} fluorescence in ORN axons.

Post-imaging analysis. Raw confocal data were analyzed in 2D using ImageJ/FIJI (RRID:SCR_002285; NIH) or in 3D using Imaris image analysis software (RRID:SCR_007370; Bitplane). Methods used for image segmentation and semi-automated quantification of fluorescent signals were previously described (Donnelly et al., 2020). Briefly, raw confocal data were cropped to establish an ROI for further analysis and displayed as a 2D sum intensity projection (ImageJ) or a 3D volume (Imaris). Background fluorescence was subtracted from raw confocal images. mCD8-GFP and HTT_{ex1}-mCherry fluorescent signals was segmented using the "Surfaces" function in Imaris (surface detail = 0.25 µm, background subtraction = 0.75 µm). Using the "split touching objects" option, seed point diameter was set to 0.85 µm. pHluorin- and tdTomato-labeled VA1lm ORN axons were quantified in central 30 × 30 pixels, 50 slice ROIs from sum intensity projections of each VA1lm glomerulus. pHluorin- and tdTomato-labeled Or83b+ ORN axons or MBN soma were quantified from central 100 × 100 pixels, 75-slice ROIs of each antennal lobe or mushroom body calyx, and background intensity was subtracted from sum intensity projections. Quantification of Toll-$6^{MIMICGFP}$ fluorescence was performed using the "Spots" function in Imaris (*xy* diameter = 0.5 µm, *z*-diameter = 1.0 µm), and glial nuclei-associated GFP-Jra signal was quantified using the "Surfaces" function to identify Repo+/GFP+ nuclei (surface detail = 0.2 µm, background subtraction = 1.6 µm, number of voxels >10).

mCherry-tagged $mHTT_{ex1}$ and GFP-tagged $wtHTT_{ex1}$ aggregates were identified and quantified as previously reported (Donnelly et al., 2020). Briefly, mCherry+ surfaces were segmented and measured in Imaris (surface detail = 0.2 µm, background subtraction = 0.45 µm, seed point diameter = 0.85 µm). Seeded $wtHTT_{ex1}$ aggregates were identified as $mHTT_{ex1}$-mCherry+ objects that overlapped with $wtHTT_{ex1}$-GFP signal. Intracellular vesicles were identified using the "Surfaces" algorithm in Imaris (surface detail = 0.2 µm, background subtraction = 0.4 µm, volume >0.001 μm^3) to segment fluorescent signals associated with lysosomes (MR+, LTR+, LAMP1-GFP+, GFP-LAMP1+, mCherry-Galectin-3+, or mCherry-Galectin-8+) or phagosomes (YRab+ or YFP-Rab+). Intracellular vesicles associated with $mHTT_{ex1}$ aggregates were identified by filtering for lysosomal or phagosomal surfaces within 0.2 µm of $mHTT_{ex1}$ objects using the "Shortest Distance" calculation in Imaris.

qPCR. Transgenic *Drosophila* were flash frozen in liquid nitrogen, and heads were collected using a microsieve with a 230 nm filter to separate bodies from heads and 170 nm filter to separate heads from appendages. Total RNA was extracted from isolated fly heads using the Zymo Direct-Zol RNA miniprep kit (Zymo Research). Extracted RNA was quantified on a Nanodrop 2000 (Thermo Fisher Scientific), and equal quantities of each sample were subjected to cDNA synthesis using the High-Capacity cDNA Reverse Transcription Kit (Applied Biosystems). qPCR was performed on a T100 Thermal Cycler with a CFX384 Real-Time System (Bio-Rad Laboratories) using 10 ng of input RNA per replicate and TB Green Premix Ex Taq II (Takara Bio). Sequences of all qPCR primers used in this study are listed in Table 3.

Experimental design and statistical analyses. All quantified data were organized and analyzed in Prism 9 software (Graphpad). Power

Table 2. Genotypes of flies used in all figures

Figure	Genotype
Figure 1*A,C–E*	*Or67d-QF/Y;QUAS-HTT$_{ex1}$Q25-mCherry/QUAS-mCD8-GFP*
Figure 1*B–E*	*Or67d-QF/Y;QUAS-HTT$_{ex1}$Q91-mCherry/QUAS-mCD8-GFP*
Figure 2*A,D,E*	*Or67d-QF/Y;UAS-HTT$_{ex1}$Q25-V5/QUAS-mCD8-GFP;repo-gal4/+*
Figure 2*B,D,E*	*Or67d-QF/Y;UAS-HTT$_{ex1}$Q91-V5/QUAS-mCD8-GFP;repo-gal4/+*
Figure 2*C*	*+/Y;UAS-HTT$_{ex1}$Q25-V5/+;repo-gal4/+ & +/Y;UAS-HTT$_{ex1}$Q91-V5/+; repo-gal4/+*
Figure 3*A,C,D*	*w1118/Y;UAS-HTT$_{ex1}$Q25-V5/Or47b-Gal4;UAS-MapHS/+*
Figure 3*B–D*	*w1118/Y;UAS-HTT$_{ex1}$Q91-V5/Or47b-Gal4;UAS-MapHS/+;*
Figure 3*C*	*w1118/Y;repo-Cas9/Or47b-Gal4;UAS-MapHS/gRNA-draper*
Figure 4*A,C*	*w1118/Y;+/+;UAS-pHluorin-HTT$_{ex1}$Q25-tdTomato/Orco-Gal4*
Figure 4*B,C*	*w1118/Y;+/+;UAS-pHluorin-HTT$_{ex1}$Q91-tdTomato/Orco-Gal4*
Figure 4*D,F*	*w1118/Y;+/+;UAS-pHluorin-HTT$_{ex1}$Q25-tdTomato/+;OK107-Gal4/+*
Figure 4*E,F*	*w1118/Y;+/+;UAS- pHluorin-HTT$_{ex1}$Q91-tdTomato/+;OK107-Gal4/+*
Figure 4*G,I*	*W1118/Y;Repo-Cas9/+;+/+*
Figure 4*H,I*	*W1118/Y;Repo-Cas9/+;gRNA-draper/+*
Figure 4*J,L*	*W1118/Y;Or47b-Gal4/repo-Cas9;+/UAS- UAS-pHluorin-HTT$_{ex1}$Q91-tdTomato*
Figure 4*J–L*	*W1118/Y;Or47b-Gal4/repo-Cas9;gRNA-draper/UAS-UAS-pHluorin-HTT$_{ex1}$Q91-tdTomato*
Figure 5*A*	*w1118; UAS-GFP/+;orco-Gal4/+ & w1118; UAS-HTT$_{ex1}$Q25-GFP/+;orco-Gal4/+ & w1118; UAS-HTT$_{ex1}$Q91-GFP/+;orco-Gal4/+*
Figure 5*C,E*	*w1118/Y; UAS-HTT$_{ex1}$Q25-V5/+;orco-Gal4/*Toll6^{MIMICGFP}
Figure 5*D,E*	*w1118/Y; UAS-HTT$_{ex1}$Q91-V5/+;orco-Gal4/*Toll6^{MIMICGFP}
Figure 5*F,H*	*w1118/Y; UAS-HTT$_{ex1}$Q25-V5/+;orco-Gal4/Jra.GFP*
Figure 5*G,H*	*w1118/Y; UAS-HTT$_{ex1}$Q91-V5/+;orco-Gal4/Jra.GFP*
Figure 6*A–H*	*w1118; UAS-HTT$_{ex1}$Q25-GFP/+;orco-Gal4/+ & w1118; UAS-HTT$_{ex1}$Q91-GFP/+;orco-Gal4/+*
Figure 7*A,C,E*	*w1118; QUAS-HTT$_{ex1}$Q25-mCherry/+;orco-QF2/+*
Figure 7*B–D, F–H*	*w1118; QUAS-HTT$_{ex1}$Q91-mCherry/+;orco-QF2/+*
Figure 8*A,C,D*	*or67d-QF,QUAS-HTT$_{ex1}$Q91-mCherry/+;QUAS-HTT$_{ex1}$Q25-GFP/+; mz0709-Gal4/+*
Figure 8*B–D*	*or67d-QF,QUAS-HTT$_{ex1}$Q91-mCherry/+;QUAS-HTT$_{ex1}$Q25-GFP/+;alrm-Gal4/+*
Figure 9*A,B,E*	(control) *or67d-QF,QUAS-HTT$_{ex1}$Q91-mCherry/+;+/+;mz0709-Gal4/+ & or67d-QF,QUAS-HTT$_{ex1}$Q91-mCherry/+;+/+;mz0709-Gal4/UAS-RNAi-X & or67d-QF,QUAS-HTT$_{ex1}$Q91-mCherry/+; UAS-RNAi-X/+;mz0709-Gal4/+*
Figure 9*C–E*	(control) *or67d-QF,QUAS-HTT$_{ex1}$Q91-mCherry/+;+/+;repo-Gal4,Gal80^{ts}/UAS-RNAi-mCherry & or67d-QF,QUAS-HTT$_{ex1}$Q91-mCherry/+;+/+; repo-Gal4,Gal80^{ts}/UAS-RNAi-Ets21c*
Figure 10*A,C,D,F*	*w1118/Y;UAS-HTT$_{ex1}$Q25-GFP/+;orco-Gal4/+*
Figure 10*B,C, E–H*	*w1118/Y;UAS-HTT$_{ex1}$Q91-GFP/+;orco-Gal4/+*
Figure 11*A,G–I*	*w1118/Y;QUAS-HTTex1Q25-mCherry/UAS-LAMP1-GFP;orco-QF2/repo-Gal4*
Figure 11*B,C, G–I*	*w1118/Y;QUAS-HTTex1Q91-mCherry/UAS-LAMP1-GFP;orco-QF2/repo-Gal4*
Figure 11*D,G–I*	*w1118/Y;QUAS-HTTex1Q25-mCherry/UAS-GFP-LAMP1;orco-QF2/repo-Gal4*
Figure 11*E–I*	*w1118/Y;QUAS-HTTex1Q91-mCherry/UAS-GFP-LAMP1;orco-QF2/repo-Gal4*
Figure 12*A,B, E–G*	Control: *QUAS-HTT$_{ex1}$Q25-GFP/+/+;repo-Gal4,orco-QF2/UAS-mCherry-LGals3 & QUAS-HTT$_{ex1}$Q91-GFP/+/+;repo-Gal4,orco-QF2/UAS-mCherry-LGals3*
Figure 12*C–G*	Control: *QUAS-HTT$_{ex1}$Q25-GFP/+/+;repo-Gal4,orco-QF2/UAS-mCherry-LGals8 & QUAS-HTT$_{ex1}$Q91-GFP/+/+;repo-Gal4,orco-QF2/UAS-mCherry-LGals8*
Figure 13*A–C*	Control*: UAS-HTT$_{ex1}$Q25-GFP/Or67d-QF,QUAS-HTT$_{ex1}$Q91-mCherry;+/+; repo-Gal4/UAS-RNAi.mCherry & UAS-HTT$_{ex1}$Q25-GFP/Or67d-QF, QUAS-mHTT-mCherry;+/+;repo-Gal4/UAS-RNAi-X* or *UAS-HTT$_{ex1}$Q25-GFP// Or67d-QF,QUAS-mHTT-mCherry/+;UAS-RNAi-X/+; repo-Gal4/+*
Figure 14*A–C*	*Or67d-QF,QUAS-HTT$_{ex1}$Q91-mCherry/+;QUAS- HTT$_{ex1}$Q25-GFP/UAS-RNAi-X; repo-Gal4/+ & Or67d-QF,QUAS-HTT$_{ex1}$Q91-mCherry/+;QUAS-HTT$_{ex1}$Q25-GFP/+;repo-Gal4/UAS-RNAi-X*
Figure 14*D,E*	*Or67d-QF,UAS-HTTex1Q25-GFP/+; GH146-Gal4,QUAS-HTTex1Q91-mCherry/+ & Or67d-QF,UAS-HTTex1Q25-GFP/+; GH146-Gal4, QUAS-HTTex1Q91-mCherry/+; drprD5/+ & Or67d-QF, UAS-HTTex1Q25-GFP/rab10{CRISPR-KO}; GH146-Gal4, QUAS-HTTex1Q91-mCherry/+ & Or67d-QF,UAS-HTTex1Q25-GFP/ rab10{CRISPR-KO}; GH146-Gal4,QUAS-HTTex1Q91-mCherry/+; drprD5/+ &*

(*Table continues.*)

Table 2. Continued

Figure	Genotype
	Or67d-QF,UAS-HTTex1Q25-GFP/rab10CRISPR; GH146-Gal4, QUAS-HTTex1Q91-mCherry/rab14{CRISPR-KO} & Or67d-QF, UAS-HTTex1Q25-GFP/rab10CRISPR; GH146-Gal4, QUAS-HTTex1Q91-mCherry/rab14{CRISPR-KO}; drprD5/+
Figure 14*F*	*UAS-HTT$_{ex1}$Q25-GFP,QUAS-HTT$_{ex1}$Q91-mCherry/Or67d-QF;+/+;repo-Gal4/+ & UAS-HTT$_{ex1}$Q25-GFP,QUAS-HTT$_{ex1}$Q91-mCherry/Or67d-QF;+/+;repo-Gal4/ UAS-RNAi-Rab10 & UAS-HTT$_{ex1}$Q25-GFP,QUAS-HTT$_{ex1}$Q91-mCherry/ Or67d-QF;UAS-draper-I/+;repo-Gal4/UAS-RNAi-Rab10*
Figure 14*G*	*w1118/ w1118;+/+;+/+ (w1118) & Rab10(CRISPR-KO)/w1118;+/+;+/+ & Rab10(CRISPR-KO)/ Rab10(CRISPR-KO);+/+;+/+*
Figure 15*A*	Controls: *w1118; UAS-GFP/+;orco-Gal4/+ & w1118; UAS-HTT$_{ex1}$Q25-GFP/+; orco-Gal4/+ & w1118; UAS-HTT$_{ex1}$Q91-GFP/+;orco-Gal4/+*
Figure 15*B,C,H,I*	*TI{TI}Rab10[EYFP]/Y;UAS-HTT$_{ex1}$Q25-V5/+;orco-Gal4/+ & TI{TI}Rab10[EYFP]/ Y;UAS-HTT$_{ex1}$Q91-V5/+;orco-Gal4/+*
Figure 15*D,E,H,I*	*w1118/Y;UAS-HTT$_{ex1}$Q25-V5/TI{TI}Rab5[EYFP];orco-Gal4/+ & w1118/Y; UAS-HTT$_{ex1}$Q91-V5/TI{TI}Rab5[EYFP];orco-Gal4/+*
Figure 15*F–I*	*w1118/Y;UAS-HTT$_{ex1}$Q25-V5/+;orco-Gal4/TI{TI}Rab7[EYFP] & w1118/Y; UAS-HTT$_{ex1}$Q91-V5/+;orco-Gal4/ TI{TI}Rab7[EYFP]*
Figure 16*A,B, G–I*	*w1118/Y;QUAS-HTTex125-mCherry/UAS-YFP-Rab10;orco-QF2,repo-Gal4/+ & w1118/Y;QUAS-HTTex1Q91-mCherry/UAS-YFP-Rab10;orco-QF2,repo-Gal4/+*
Figure 16*C,D, G–I*	*w1118/Y;QUAS-HTTex125-mCherry/UAS-YFP-Rab5;orco-QF2,repo-Gal4/+ & w1118/Y;QUAS-HTTex1Q91-mCherry/UAS-YFP-Rab5;orco-QF2,repo-Gal4/+*
Figure 16*E–I*	*w1118/Y;QUAS-HTTex125-mCherry/UAS-YFP-Rab7;orco-QF2,repo-Gal4/+ & w1118/Y;QUAS-HTTex1Q91-mCherry/UAS-YFP-Rab7;orco-QF2,repo-Gal4/+*
Figure 17*A*1–3	*w1118/Y;QUAS-HTTex1Q91-mCherry/UAS-YFP-Rab10;orco-QF2,repo-Gal4/+*
Figure 17*B*1,2	*w1118/Y;QUAS-HTTex1Q91-mCherry/UAS-YFP-Rab5;orco-QF2,repo-Gal4/+*
Figure 17*C*1,2	*w1118/Y;QUAS-HTTex1Q91-mCherry/UAS-YFP-Rab7;orco-QF2,repo-Gal4/+*

Table 3. Primer sequences used for qPCR analyses

Gene target	Forward (F) and reverse (R) primer sequences (5′-3′)
rpl32	F: CCGCTTCAAGGGACAGTATCTG R: ATCTCGCCGCAGTAAACGC
toll-6	F: AATATTGTGGAGTGCTCGGG R: GCGTTTAAGGCCACTGAAAG
Dorsal	F: ATGCGAGCGGTGTTCAGTAA R: ACGATGCGAAAAGCCAGTCT
relish	F: ACAGGACCGCATATCG R: GTGGGGTATTTCCGGC
draper-I	F: TGTGATCATGGTTACGGAGGAC R: CAGCCGGGTGGGCAA
mmp1	F: GAAGGCTCGGACAACGAGT R: GTCGTTGGACTGGTGATCG
ets21c	F: CAACGACGACGAACCAAAT R: GTTCGCGTTGGACGAATC
rab10	F: ACATCCGCCAAGTCGAACAT R: CTGGTTCCGGCGATCGATAA
rab5	F: AGTCCGCTGTGGGCAAGTC R: CTCCTGGTACTCGTGGAACTGTC
rab7	F: AATTTTGCACGCAACCGCTG R: GAGTAGCCAATTCGATGGTGC
drosomycin	F: GCTGTCCTGATGCTGGTGGT R: CGGAAAGGGACCCTTGTATCTTC
attacin-a	F: CTCGTTTGGATCTGACCAAGG R: CCATGACCAGCATTGTTGTAG
attacin-d	F: CGTTGAGGTTGAGATTGCCACT R: CGGTCCCTCAGTTCGGCATGAC
diptericinA	F: CCACCGCAGTACCCACTCAAT R: CGATGACTGCAAAGCCAAAACCA
metchnikowin	F: CAGTGCTGGCAGAGCCTCAT R: CGTCGGTTAGGATTGAAGGGCGA

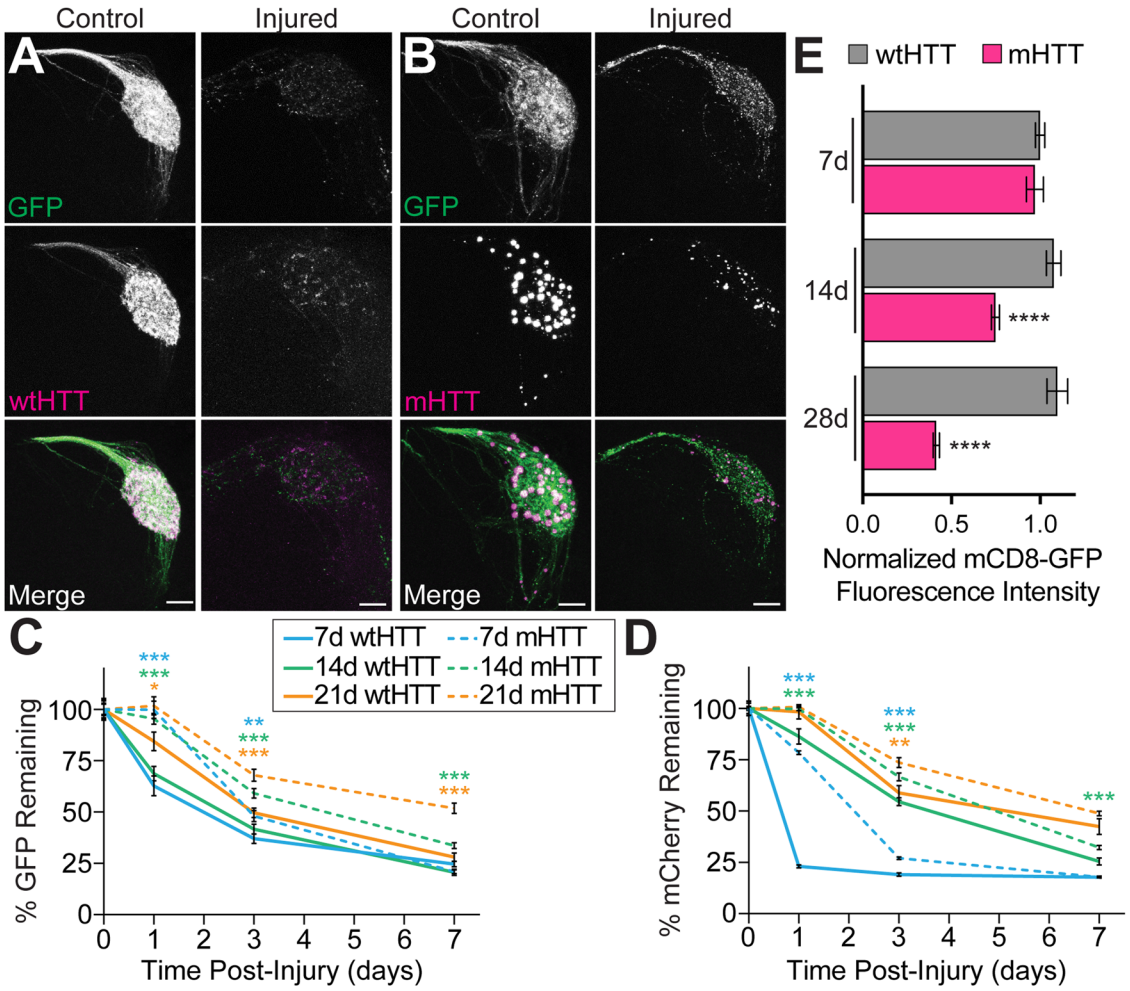

Figure 1. $mHTT_{ex1}$ expression in ORNs impairs clearance of injured axons. ***A,B***, Maximum intensity projections of mCD8-GFP-labeled DA1 ORN axons expressing (***A***) $HTT_{ex1}Q25$- ($wtHTT_{ex1}$) or (***B***) $HTT_{ex1}Q91$-mCherry ($mHTT_{ex1}$) in 7-day-old uninjured flies (*left*) or 14-day-old flies subjected to bilateral antennal nerve axotomy 7 d earlier (*right*). Scale bars = 5 µm. ***C,D***, Quantification of (***C***) mCD8-GFP+ and (***D***) HTT_{ex1}-mCherry+ DA1 ORN axons remaining in 7-, 14-, and 28-day-old uninjured flies or flies at 1, 3, and 5 d postinjury. ***E***, Quantification of mCD8-GFP+ DA1 ORN axons in 7-, 14-, and 28-day-old flies expressing $HTT_{ex1}Q25$- or $HTT_{ex1}Q91$-mCherry in DA1 ORNs. All quantified data were normalized to uninjured 1-day-old adults and graphed as mean ± SEM; $*p < 0.05$, $**p < 0.01$, $***p < 0.001$, $****p < 0.0001$ by unpaired two-tailed *t* test.

analyses to determine appropriate sample sizes for each experiment were calculated using a Sample Size calculator available at ClinCalc.com ($\alpha = 0.05$, $\beta = 0.2$). All quantifications are graphed as mean ± standard error of the mean (SEM). A single glomerulus or antennal lobe represented one biological replicate. Statistical comparisons were performed using the following tests where appropriate: unpaired, two-tailed *t* test when comparing two samples and ANOVA followed by post hoc multiple-comparisons tests when comparing ≥3 samples. Detailed statistical information for each experiment, including sample sizes (*n*), means, and test results are summarized in Extended Data Tables 1–16.

Results

Expression of mHTT exon 1 fragments in neurons inhibits phagocytic clearance of axonal debris

HD is a monogenic neurodegenerative disease caused by expansion of a CAG repeat region in exon 1 of the *huntingtin* (*HTT/IT15*) gene beyond a pathogenic threshold of 37 repeats, leading to production of mHTT proteins containing expanded N-terminal polyglutamine (polyQ ≥ 37) tracts (Scherzinger et al., 1999). mHTT proteins are prone to misfolding and accumulate into insoluble aggregates (Wanker, 2000), whereas wild-type HTT (wtHTT) proteins containing polyQ ≤ 36 tracts remain soluble unless seeded by a preformed HTT aggregate (Preisinger et al., 1999; S. Chen et al., 2001). To recapitulate these molecular features of HD, we generated transgenic flies that express N-terminal exon 1 fragments of human mHTT ($mHTT_{ex1}$) containing a polyQ91 tract or wtHTT ($wtHTT_{ex1}$) with a polyQ25 tract via the GAL4-UAS (Brand and Perrimon, 1993) or QF-QUAS binary expression systems (Potter and Luo, 2011). As we have previously reported (Pearce et al., 2015; Donnelly et al., 2020), fluorescent protein fusions of $mHTT_{ex1}$ and $wtHTT_{ex1}$ appeared punctate (i.e., aggregated or insoluble) or diffuse (i.e., soluble), respectively, in axon termini of the DA1 type of olfactory receptor neurons (ORNs), which synapse in the DA1 glomerulus of the antennal lobe in the central brain of adult flies (Couto et al., 2005; Fig. 1*A,B*).

To monitor the capacity of glia to maintain CNS homeostasis in the presence of $mHTT_{ex1}$ aggregates, we performed a series of experiments that quantified glial responses to acute injury in the adult fly CNS. Surgical removal of the second and third antennal segments initiates Wallerian degeneration of ORN axons, inducing a robust phagocytic glial response that involves upregulation of the scavenger receptor, Draper, and clearance of axonal debris within 7 d (MacDonald et al., 2006). To determine if neuronal

$mHTT_{ex1}$ expression affects the ability of glial cells to efficiently clear axonal debris, we coexpressed mCherry-tagged HTT_{ex1} transgenes with membrane-targeted GFP (mCD8-GFP) in DA1 ORNs and measured GFP and mCherry fluorescence intensities following antennal nerve axotomy (Fig. 1*A–D*). Interestingly, $mHTT_{ex1}$ expression was associated with reduced steady-state mCD8-GFP levels in DA1 ORN axons in 2 and 4 week old flies (Fig. 1*E*), likely due to neurotoxicity caused by accumulation of $mHTT_{ex1}$ aggregates over time. Quantification of DA1 ORN axons remaining after antennal nerve injury revealed that clearance of axonal debris was reduced in flies coexpressing neuronal $mHTT_{ex1}$ compared with controls expressing $wtHTT_{ex1}$ (Fig. 1*C*). This effect could be observed as early as 1 d post-injury, suggesting that $mHTT_{ex1}$ causes defects in both clearance and engulfment of axonal debris. Delayed clearance of axonal debris was exacerbated in older (14- and 28-day-old) $mHTT_{ex1}$-expressing flies (Fig. 1*C*), possibly related to a decline in Draper activity during normal aging (Purice et al., 2016) and/or enhanced glial dysfunction compounded by $mHTT_{ex1}$ aggregate accumulation. Quantification of mCherry fluorescence indicated that clearance of axonal $mHTT_{ex1}$ was also slowed compared to $wtHTT_{ex1}$ (Fig. 1*D*), suggesting that glia are deficient in degrading both axonal debris and neuronal $mHTT_{ex1}$ aggregates.

We also tested whether formation of $mHTT_{ex1}$ aggregates in glial cells impacts ORN axonal debris clearance following acute injury. Restricting expression of $mHTT_{ex1}$ to glia resulted in appearance of heterogeneously sized $mHTT_{ex1}$ aggregates throughout the brain (Fig. 2*A*). Glial $mHTT_{ex1}$ aggregates also slowed injury-induced clearance of mCD8-GFP-labeled axons compared with $wtHTT_{ex1}$-expressing controls (Fig. 2*B–D*), though glial $mHTT_{ex1}$ expression did not affect DA1 ORN axon abundance in 1-day-old flies (Fig. 2*E*). Together, these findings indicate that $mHTT_{ex1}$ aggregates originating in either neurons or glia slow efficient clearance of injured ORN axons by phagocytic glia.

Neuronal mHTT aggregates impair nascent phagosome formation

Phagocytosis occurs via four major steps: (1) extension of phagocyte membranes toward extracellular "find me" cues, (2) recognition of "eat me" signals by scavenger receptors, (3) cytoskeletal and plasma membrane reorganization to surround and internalize extracellular material, and (4) maturation of nascent phagosomes through sequential endomembrane fusions that culminate at the lysosome (Vieira et al., 2002). We have previously reported that the conserved scavenger receptor, Draper/Ced-1/MEGF10 (MacDonald et al., 2006; Evans et al., 2015; Iram et al., 2016), regulates engulfment, clearance, and intercellular spreading of $mHTT_{ex1}$ aggregates originating in ORN axons (Pearce et al., 2015; Donnelly et al., 2020). To determine whether delayed clearance of injured axons containing $mHTT_{ex1}$ aggregates (Figs. 1*C*, 2*D*) could result from defective Draper-dependent engulfment, we coexpressed V5-tagged $mHTT_{ex1}$ or $wtHTT_{ex1}$ with the ratiometric membrane-associated pH sensor (MApHS), consisting of the transmembrane domain of CD4 flanked by N-terminal ecliptic pHluorin and C-terminal tdTomato (Han et al., 2014), in the VA1lm type of ORNs. Ecliptic pHluorin is brightest at pH 7.5 and dims as pH drops, quenching at pH < 6.0 (Miesenböck et al., 1998), whereas tdTomato fluorescence is pH resistant. Thus, internalization of MApHS-labeled ORN axonal debris into a rapidly acidified nascent phagosome can be monitored by calculating pHluorin/tdTomato fluorescence intensity ratios (Han et al., 2014). Indeed, pHluorin/tdTomato ratios in VA1lm axons were decreased at 14 and 25 h postaxotomy (Fig. 3*A–C*), and this effect was lost when *draper* was deleted from glia using the tissue-specific CRISPR/Cas9-TriM method (Fig. 3*C,E–G*; Poe et al., 2019), demonstrating that this construct accurately reports nascent phagosome acidification following engulfment. Notably, the decrease in pHluorin/tdTomato ratio following injury was less pronounced in VA1lm ORN axons coexpressing $mHTT_{ex1}$ compared with $wtHTT_{ex1}$-expressing controls (Fig. 3*A–C*), suggesting that $mHTT_{ex1}$ aggregates impair nascent phagosome formation following engulfment.

Neuronal mHTT accumulates in low pH intracellular compartments

$mHTT_{ex1}$ expression was associated with a slight but significant decrease in steady-state pHluorin/tdTomato ratios in MApHS-labeled axons compared with $wtHTT_{ex1}$-expressing controls (Fig. 3*D*), suggesting that even in the absence of acute injury, $mHTT_{ex1}$ signals for ORN axon engulfment. To test this, we generated transgenic flies that express $mHTT_{ex1}$ or $wtHTT_{ex1}$ fused to N-terminal pHluorin and C-terminal tdTomato fluorescent proteins, herein referred to as mHTT-associated pH sensor (mHApHS) or wtHTT-associated pH sensor (wtHApHS). Accumulation of HTT_{ex1} protein in low pH cellular compartments would cause a decrease in the ratio of pHluorin/tdTomato fluorescence for these constructs.

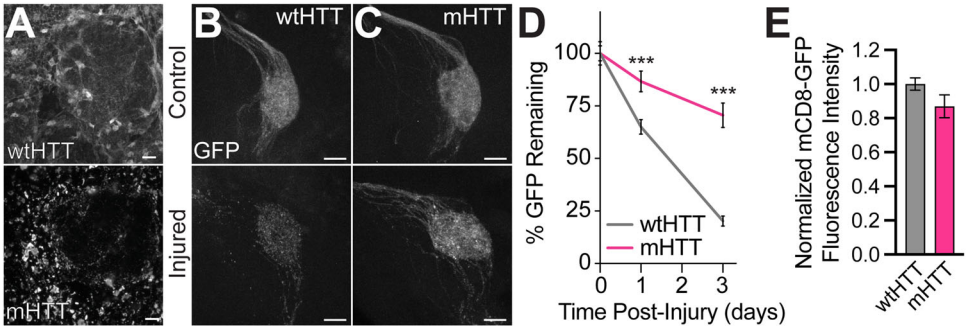

Figure 2. $mHTT_{ex1}$ expression in glia is associated with reduced ORN axon clearance postinjury. ***A,B***, Maximum intensity projections of antennal lobes from 5- to 6-day-old flies expressing HTT_{ex1}Q25- (*top*) or HTT_{ex1}Q91-V5 (*bottom*) in glia and immunostained with anti-V5. Scale bars = 10 µm. ***B,C***, Maximum intensity projections of mCD8-GFP-labeled DA1 ORN axons in 1-day-old flies expressing (***B***) HTT_{ex1}Q25- or (***C***) HTT_{ex1}Q91-V5 in repo+ glia. Scale bars = 5 µm. ***D***, Quantification of mCD8-GFP+ DA1 ORN axons in flies expressing HTT_{ex1}Q25- or HTT_{ex1}Q91-V5 in repo+ glia, either uninjured or at 1 and 3 d postinjury. ***E***, Quantification of mCD8-GFP+ DA1 ORN axons in 1-day-old flies expressing HTT_{ex1}Q25- or HTT_{ex1}Q91-mCherry in repo+ glia. All data were normalized to uninjured 1-day-old adult flies and graphed as mean ± SEM; ***$p < 0.001$ by unpaired two-tailed *t* test.

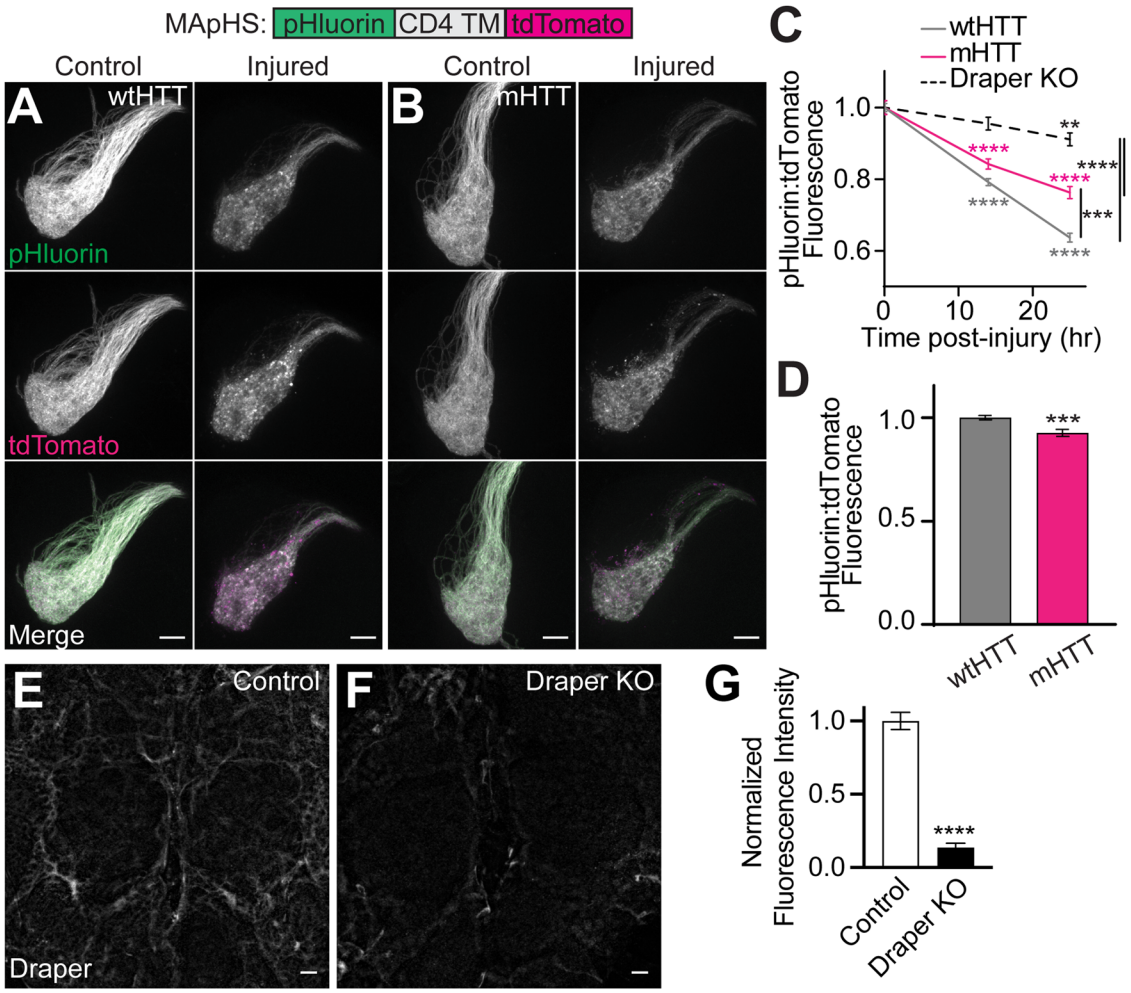

Figure 3. $mHTT_{ex1}$ expression inhibits engulfment of injured ORN axons. ***A,B***, Maximum intensity projections of VA1lm ORN axons coexpressing the ratiometric phagocytic indicator, MApHS, and (***A***) HTT_{ex1}Q25- or (***B***) HTT_{ex1}Q91-V5 from 7-day-old uninjured flies (*left*) and flies 25 h postinjury (*right*). Scale bars = 10 µm. ***C***, pHluorin:tdTomato fluorescence intensity ratios calculated in VA1lm glomeruli from 7-day-old uninjured flies and flies at 14 or 25 h postinjury. Data were normalized to the uninjured condition for each genotype. ***D***, pHluorin:tdTomato fluorescence intensity ratios in 7-day-old flies coexpressing MApHS with HTT_{ex1}Q25- or HTT_{ex1}Q91-V5 in VA1lm ORNs, normalized to $wtHTT_{ex1}$ controls. Data are shown as mean ± SEM; $^{**}p < 0.01$, $^{***}p < 0.001$, $^{****}p < 0.0001$ by unpaired two-tailed *t* test. ***E,F***, Maximum intensity projections of the central brain from 6 to 7-day-old flies expressing (***E***) repo-Cas9 or (***F***) repo-Cas9 plus gRNAs targeting *draper* ("Draper KO"). Brains were immunostained with anti-Draper. Scale bars = 10 µm. ***G***, Quantification of Draper immunofluorescence in brains from flies shown in (***E,F***), normalized to control.

wtHApHS and mHApHS transgenes were expressed in either Or83b+ ORNs, which encompass 70–80% of all adult ORNs (Fig. 4*A,B*; Larsson et al., 2004), or mushroom body neurons (MBNs; Fig. 4*D,E*), which are downstream in the fly olfactory circuit and innervate the learning and memory center of the fly CNS (McGuire et al., 2001). In both ORN axons and MBN soma, pHluorin/tdTomato ratios associated with mHApHS were significantly decreased compared with wtHApHS controls (Fig. 4*C, F*), suggesting that $mHTT_{ex1}$ proteins accumulate in acidified cellular compartments. To discriminate $mHTT_{ex1}$ proteins engulfed by glia from $mHTT_{ex1}$ internalized into neuronal autophagolysosomes, we measured VA1lm ORN axonal mHApHS-associated fluorescence in animals with glial *draper* loss-of-function (Fig. 4*G,H*). Glial *draper* knockout increased pHluorin/tdTomato ratios for axonal mHApHS (Fig. 4*I*), suggesting that at least some portion of $mHTT_{ex1}$ aggregates accumulate in acidic portions of the glial phagolysosomal system.

Neuronal mHTT impairs injury-responsive gene upregulation

Glia alter their transcriptional profile to elicit cellular responses to insult or injury in the brain. For example, acute CNS injury in *Drosophila* increases transcription of many genes involved in phagocytosis and innate immunity, including the cell surface receptors, Draper and Toll-6, and components of their downstream signaling pathways (Fig. 5*A*; Purice et al., 2017; Byrns et al., 2021; van Alphen et al., 2022). To test whether the reduced ability of glia to clear $mHTT_{ex1}$ -containing axonal debris correlates with reduced injury responsiveness at a transcriptional level, we used qPCR and GFP-tagged reporters to quantify changes in gene expression of key components of these phagocytic and innate immunity pathways following $mHTT_{ex1}$ accumulation in neurons. $mHTT_{ex1}$ expression in uninjured Or83b+ ORNs increased relative expression of *toll-6*, *relish*, and *drpr-I* transcripts between 1.2- and 1.5-fold (Fig. 5*B*) and levels of GFP-tagged Toll-6 and Jra proteins in the CNS (Fig. 5*C–H*), suggesting that neuronal $mHTT_{ex1}$ aggregates activate a mild injury response in the brain. Jra-GFP expression increased throughout the CNS and in Repo+ nuclei (Fig. 5*F–H*), suggesting that $mHTT_{ex1}$-induced upregulation of this subunit of the AP-1 transcription factor can be at least partially attributed to glia. To test whether $mHTT_{ex1}$ impairs the ability of glia to respond to acute neural injury, we monitored gene expression changes after

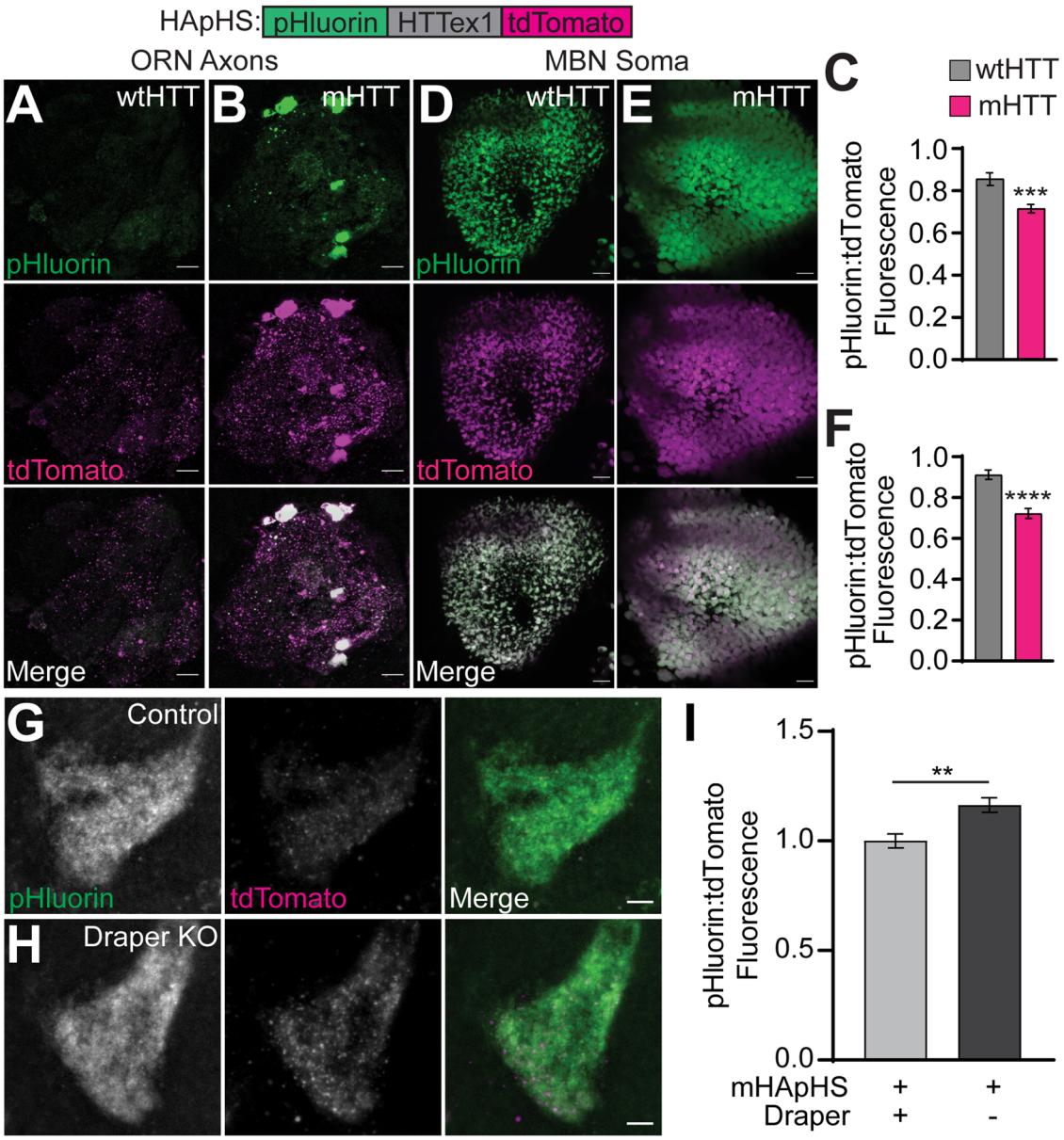

Figure 4. Neuronal $mHTT_{ex1}$ accumulates in acidic cellular compartments. ***A,B,D,E***, Maximum intensity projections of (***A,B***) Or83b+ ORN axons or (***D,E***) OK107+ MBN soma expressing (***A,D***) HTT_{ex1}Q25- or (***B,E***) HTT_{ex1}Q91-associated pH sensor (HApHS) from 13- to 14-day-old flies. Scale bars = 10 µm. ***C,F***, pHluorin:tdTomato fluorescence intensity ratios of data shown in (***A,B,D,E***), normalized to $wtHTT_{ex1}$ controls. ***G,H***, Maximum intensity projections of VA1lm ORN axons coexpressing mHApHS and (***G***) repo-Cas9 or (***H***) repo-Cas9 and gRNAs targeting *draper*. Scale bars = 5 µm. ***I***, pHluorin:tdTomato fluorescence intensity ratios calculated in VA1lm glomeruli from 9- to 10-day-old flies as shown in (***G,H***). Data were normalized to flies not expressing gRNAs. All quantified data are shown as mean ± SEM; $^{**}p < 0.01$, $^{***}p < 0.001$, $^{****}p < 0.0001$ by unpaired two-tailed *t* test.

bilateral antennal and maxillary palp nerve ablation. Similar to previous reports (Purice et al., 2017), expression of *toll-6*, *dorsal*, *relish*, *drpr-I*, *mmp1*, and *ets21c* genes was significantly increased 3 h after injury to ORN axons expressing either mCD8-GFP or $wtHTT_{ex1}$ (Fig. 5*B*). However, injury-induced upregulation of each of these genes was significantly reduced in animals expressing $mHTT_{ex1}$ in Or83b+ ORNs (Fig. 5*B*), suggesting that $mHTT_{ex1}$ aggregation attenuates glial transcriptional responses to injury. We further analyzed the impact of $mHTT_{ex1}$ on downstream immune responses in the brain by measuring induction of antimicrobial peptide (AMP) genes, well-established transcriptional targets of activated Relish/NFκB following Toll-6 or immune-deficiency pathway activation (Swanson et al., 2020a,b; van Alphen et al., 2022). Transcription of five AMP, including *drosomycin*, *attacinA*, *attacinD*, *diptericinA*, and *metchnikowin*, was significantly increased 3 h after ORN axotomy (Fig. 6*A–E*), similar to previous reports (Katzenberger et al., 2013; Swanson et al., 2020b; Marischuk et al., 2021). Interestingly, $mHTT_{ex1}$ expression in ORNs alone was sufficient to induce upregulation of *drosomycin* and *attacinD* (Fig. 6*A,C*), albeit to a lesser extent than following acute injury. Further, injury-induced upregulation of *drosomycin* and *attacinA* was significantly reduced by $mHTT_{ex1}$ expression in ORNs, suggesting that the activity of Relish-dependent signaling is altered by accumulation of $mHTT_{ex1}$ aggregates. Together, these data indicate that neuronal $mHTT_{ex1}$ aggregates trigger a mild immune response in the brain, but also inhibit the ability of glia to mount robust transcriptional responses to neural injury.

Our findings are in agreement with previously published work demonstrating that expression of $mHTT_{ex1}$ and Aβ in neurons

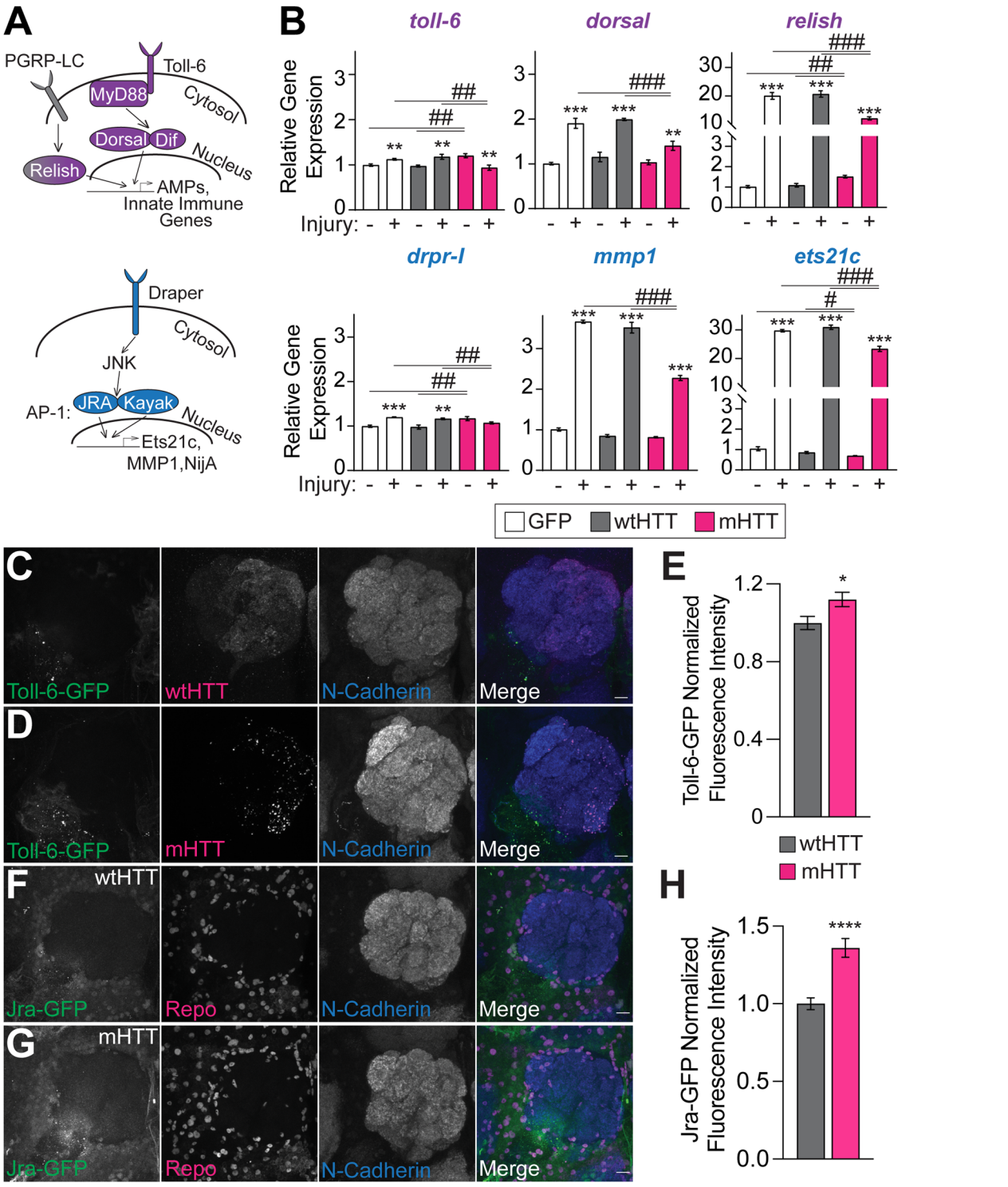

Figure 5. $mHTT_{ex1}$ expression in ORNs upregulates phagocytic and innate immunity genes and impairs injury-induced transcriptional responses. ***A***, Diagrams of Toll-6 (purple) and Draper (blue) signaling pathways. ***B***, qPCR analysis of the indicated genes in 8- to 11-day-old flies expressing GFP, HTT_{ex1}Q25-, or HTT_{ex1}Q91-GFP in Or83b+ ORNs. RNA was isolated from heads of uninjured flies or flies 3 h after bilateral antennal and maxillary palp nerve injury. Data are shown as mean ± SEM and normalized to the housekeeping gene *rpl32*. *$p < 0.05$, **$p < 0.01$, ***$p < 0.001$ by one-way ANOVA; asterisks and hashtags indicate statistical significance comparing ± injury or genotypes, respectively. ***C,D,F,G***, Maximum intensity projections of Or83b+ ORN axons from 14- to 15-day-old flies expressing (***C,F***) HTT_{ex1}Q25- or (***D,G***) HTT_{ex1}Q91-V5 in (***C,D***) Toll-$6^{MIMICGFP}$ (Toll-6-GFP) or (***F,G***) Jra-GFP genetic backgrounds. Brains were immunostained with GFP, V5, and N-Cadherin (***C,D***) or GFP, Repo, and N-Cadherin (***F,G***) antibodies. In panel (***C***), diffuse $wtHTT_{ex1}$ signal was adjusted postacquisition for increased visibility. Scale bars = 10 µm. ***E,H***, Quantification of (***E***) Toll-6-GFP or (***H***) Jra-GFP expression from flies show in (***C,D,F,G***). Data are graphed as mean ± SEM; *$p < 0.05$, ****$p < 0.0001$ by unpaired two-tailed *t* test.

activates Draper-dependent phagocytosis, likely in an effort to reduce levels of these pathogenic proteins in the brain (Pearce et al., 2015; Ray et al., 2017). We further investigated this by immunostaining adult fly brains expressing $mHTT_{ex1}$ in ORNs to monitor expression levels and localization of endogenous Draper protein. In 1 week old adult flies expressing neuronal $mHTT_{ex1}$, Draper immunolabeling increased ~1.2-fold in the vicinity of ORN axons compared with age-matched controls

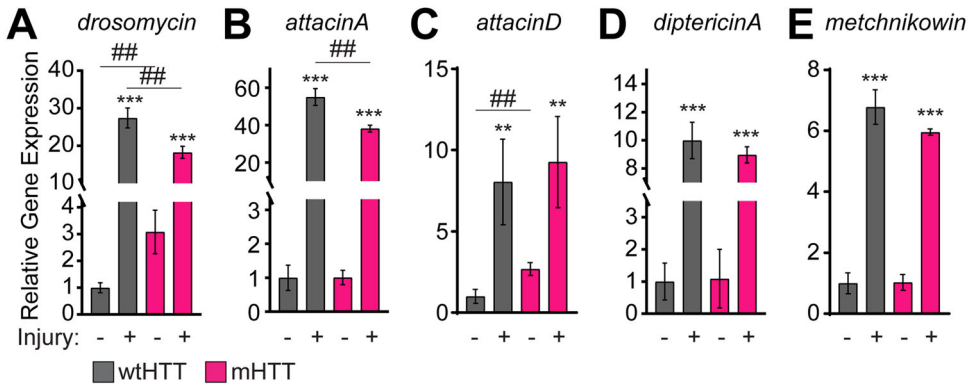

Figure 6. $mHTT_{ex1}$ expression in ORNs upregulates and impairs injury-induced upregulation of some AMP genes. ***A–E***, qPCR analysis of the indicated genes in 8- to 11-day-old flies expressing HTT_{ex1}Q25- or HTT_{ex1}Q91-GFP in Or83b+ ORNs. RNA was isolated from heads of uninjured flies or flies 3 h after bilateral antennal and maxillary palp nerve injury. Data are shown as mean ± SEM and normalized to the housekeeping gene *rpl32*. $^{**}p < 0.01$, $^{***}p < 0.001$ by unpaired two-tailed *t* test; asterisks and hashtags indicate statistical significance comparing ± injury or genotypes, respectively.

expressing $wtHTT_{ex1}$ (Fig. 7*A–C*). Closer analysis revealed that in some cases, Draper immunofluorescence was directly adjacent to or surrounding $mHTT_{ex1}$-mCherry fluorescence (Fig. 7*D*). To further examine these interactions, we used image segmentation and three-dimensional reconstruction of confocal stacks to represent $mHTT_{ex1}$-mCherry+ aggregates and Draper+ glial membranes as individual "surfaces" (Fig. 7*E,F*), as previously described (Donnelly et al., 2020). Close physical association of $mHTT_{ex1}$ with Draper and other glial proteins was defined as surfaces located ≤0.2 µm from a $mHTT_{ex1}$ object. Interestingly, whereas almost no Draper signal was detected near $wtHTT_{ex1}$ (Fig. 7*E*), ∼14% of $mHTT_{ex1}$ aggregates were closely associated with Draper surfaces (Fig. 7*F*1–3). These findings are consistent with Draper+ glial membranes being recruited to neuronal $mHTT_{ex1}$ aggregates to facilitate engulfment.

Synaptic neuropil in the *Drosophila* brain is primarily inhabited by two glial subtypes, ensheathing glia and astrocytic glia (Doherty et al., 2009). In adult flies, ensheathing glia compartmentalize synaptic regions and respond to CNS injury by upregulating Draper and clearing debris via phagocytosis (Doherty et al., 2009). Consistent with our previous findings in all repo+ glia (Pearce et al., 2015), mz0709+ ensheathing glia were vulnerable to prion-like conversion of glial $wtHTT_{ex1}$ proteins by $mHTT_{ex1}$ aggregates generated in DA1 ORN axons (Fig. 8*A,C,D*). Seeded $wtHTT_{ex1}$ aggregates were defined as $wtHTT_{ex1}$ signal that colocalized with $mHTT_{ex1}$ objects identified by image segmentation of confocal stacks (Donnelly et al., 2020). Conversely, seeding of $wtHTT_{ex1}$ expressed in alrm+ astrocytic glia, which lack detectable Draper expression in the adult fly brain (Doherty et al., 2009), was not observed (Fig. 8*B–D*). Interestingly, ensheathing glial-specific RNAi knockdown of Toll-6, Relish, and NijA increased $mHTT_{ex1}$ aggregate numbers in DA1 ORN axons, similar to the effects of Draper-I knockdown (Fig. 9*A,B*). Further, adult-specific, pan-glial knockdown of Ets21c, which was found to be required for normal development, also increased numbers of $mHTT_{ex1}$ aggregates in DA1 ORN axons (Fig. 9*C,D*). Mean $mHTT_{ex1}$ aggregate volume was not affected by ensheathing glial knockdown of these genes, except for a ∼20% increase following NijA depletion (Fig. 9*E*), suggesting that neither aggregate nor vesicle size was unaffected by these genetic manipulations. Thus, several glial genes with established roles in phagocytic and innate immune signaling regulate basal turnover of $mHTT_{ex1}$ aggregates in ORN axons.

Neuronal mHTT aggregates are associated with defects in multiple endolysosomal compartments

Our findings thus far indicate that neuronal $mHTT_{ex1}$ aggregates elicit mild injury responses in the brain and reduce the ability of phagocytic glia to respond transcriptionally and functionally to acute nerve injury. We have previously postulated that prion-like spreading of $mHTT_{ex1}$ in the fly CNS could be facilitated by escape of engulfed aggregates from the endolysosomal compartment of phagocytic glia (Pearce et al., 2015; Donnelly et al., 2020). Therefore, we sought to determine whether neuronal $mHTT_{ex1}$ aggregates are associated with defects in endolysosomal processing in uninjured brains. We first measured effects of neuronal $mHTT_{ex1}$ expression on the quantity, size, and function of lysosomes using dyes that label active cathepsins and low pH cellular compartments. Expression of $mHTT_{ex1}$ in Or83b+ ORNs increased numbers of lysosomes labeled by the active cathepsin dye, Magic Red (MR) (Fig. 10*A–C*), and the low pH sensor, LysoTracker Red (LTR) (Fig. 10*D–F*), compared with control brains expressing $wtHTT_{ex1}$. High resolution analysis of confocal stacks and filtering for segmented MR+ and LTR+ surfaces within 0.2 µm of a $mHTT_{ex1}$ object revealed close association of MR+ and LTR+ signals with $mHTT_{ex1}$ aggregates (Fig. 10*C,F–H*).

We next employed *Drosophila* genetic tools to assess the impact of neuronal $mHTT_{ex1}$ specifically on glial lysosomes by driving expression of lysosomal-associated membrane protein 1 (LAMP1) tagged at its cytosolic C-terminus with GFP (LAMP1-GFP) in all glia. Neuronal $mHTT_{ex1}$ expression increased the overall number of glial LAMP1-GFP+ vesicles and the number of LAMP1-GFP+ vesicles in close proximity to HTT_{ex1} signal (Fig. 11*A–C,G,H*). We typically observed only partial overlap of LAMP1-GFP signal with $mHTT_{ex1}$ aggregate surfaces identified by this method, possibly due to incomplete labeling or rupture of lysosomal membranes as a result of aggregate size or structural features. Interestingly, this subpopulation of LAMP1-GFP+ lysosomes closely associated with $mHTT_{ex1}$ were enlarged compared with all lysosomes (Fig. 11*I*). To examine whether neuronal $mHTT_{ex1}$ aggregates affect lysosome integrity, we expressed a transgene encoding LAMP1 fused at its N-terminus to GFP in glia. This construct integrates into the lysosomal membrane such that GFP is exposed to the lumen, and loss of GFP signal can thus be used to monitor LAMP1+ lysosome degradative activity (Pulipparacharuvil et al., 2005). Interestingly, the quantity and mean volume of GFP-LAMP1+ vesicles were significantly

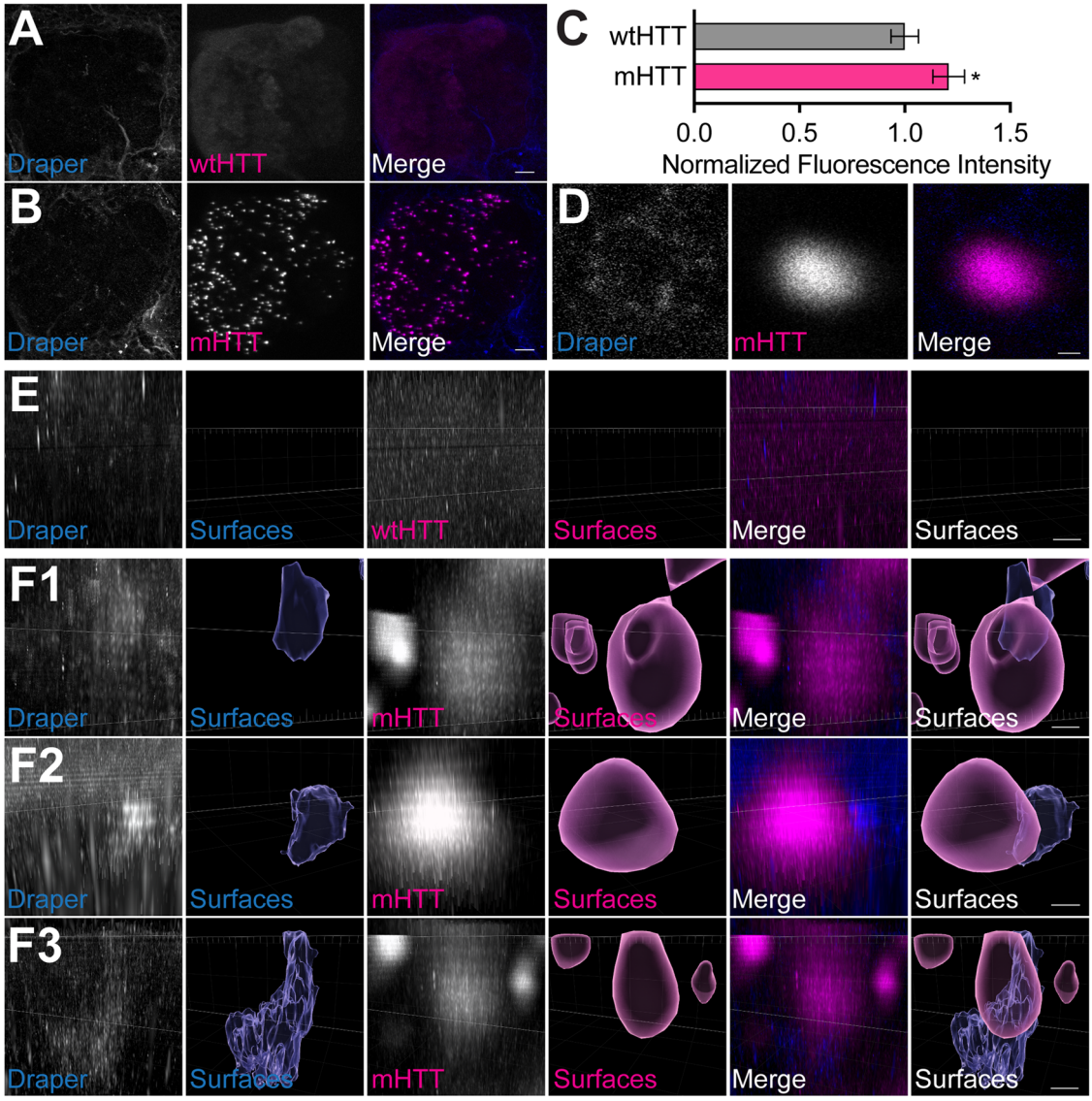

Figure 7. A subset of $mHTT_{ex1}$ aggregates are closely associated with Draper+ glial membranes. ***A,B***, Maximum intensity projections of Or83b+ ORN axons from 7- to 8-day-old flies expressing (***A***) HTT_{ex1}Q25- or (***B***) HTT_{ex1}Q91-mCherry and immunostained for Draper. Scale bars = 10 µm. ***C***, Quantification of Draper immunofluorescence from flies shown in (***A,B***). Data are normalized to control and graphed as mean ± SEM; $*p < 0.05$ by unpaired two-tailed *t* test; $n = 12$. ***D***, Single 0.35 µm confocal slice showing a magnified HTT_{ex1}Q91-mCherry aggregate and closely-associated Draper signal. Scale bar = 0.5 µm. ***E,F***, High-magnification confocal stacks of Draper signal within 0.2 µm of either (***E***) HTT_{ex1}Q25- or (***F1–3***) HTT_{ex1}Q91-mCherry surfaces. Raw data are shown to the left of segmented surfaces generated from each fluorescence signal. In (***E***), diffuse $wtHTT_{ex1}$ signal was adjusted postacquisition for increased visibility. Scale bars = 1 µm.

increased in brains expressing $mHTT_{ex1}$ in Or83b+ ORNs (Fig. 11*D–G*), suggesting lysosomal enlargement and dysfunction due to $mHTT_{ex1}$ aggregates. GFP-LAMP1+ surfaces were also more associated with $mHTT_{ex1}$ aggregates compared to $wtHTT_{ex1}$ controls (Fig. 11*F,I*).

To directly test whether glial endolysosomes experience membrane damage due to neuronal $mHTT_{ex1}$ expression, we generated transgenic flies expressing mCherry-tagged Galectin-3 or Galectin-8, lectins that translocate from the cytoplasm to the lumen of ruptured lysosomes and endosomes, respectively (Aits et al., 2015; Daussy and Wodrich, 2020; Jia et al., 2020). Neuronal $mHTT_{ex1}$ expression increased overall numbers of glial Galectin-3/8+ surfaces (Fig. 12*A–E*), Galectin-3/8+ surfaces closely associated with $mHTT_{ex1}$ aggregates (Fig. 12*F*), and mean volume of $mHTT_{ex1}$-associated Galectin-3/8+ vesicles (Fig. 12*G*). Together, these data suggest that neuronal $mHTT_{ex1}$ aggregates induce non cell-autonomous accumulation, enlargement, and membrane damage of endolysosomal vesicles in glial cells.

"Seeding-competent" mHTT aggregates are defined by their ability to nucleate or "seed" the aggregation of normally soluble wtHTT proteins, analogous to how infectious prions and other prion-like proteins replicate (Jucker and Walker, 2018; Donnelly et al., 2022). Many studies have pointed to a role for defective clearance by endolysosomal pathways in promoting the propagation of pathogenic aggregates (Freeman et al., 2013; Jiang et al., 2017; J. J. Chen et al., 2019; Jiang and Bhaskar, 2020; Polanco and Götz, 2022). To test whether altered glial lysosome function affects seeding competency of $mHTT_{ex1}$, we used RNAi to individually knockdown proteins with known roles in lysosome degradation in glia and examined the ability of neuronal mCherry-tagged $mHTT_{ex1}$ to seed aggregation of glial, GFP-tagged $wtHTT_{ex1}$. Depletion of two subunits of the vacuolar ATPase (V-ATPase), Vha68-3 (Portela et al., 2018) and

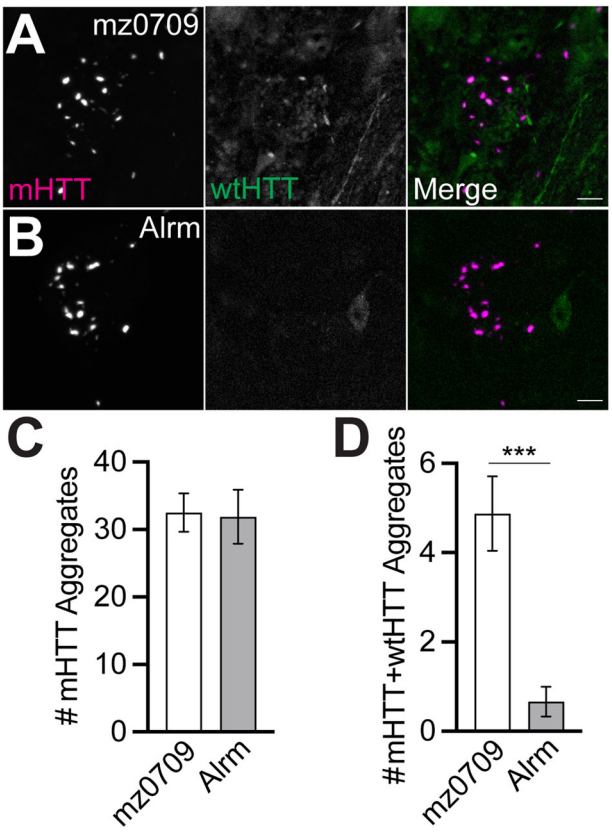

Figure 8. Seeded aggregation of $wtHTT_{ex1}$ in ensheathing glia by neuronal $mHTT_{ex1}$ aggregates. ***A,B***, Maximum intensity projections of DA1 glomeruli from 4- to 5-day-old flies expressing HTT_{ex1}Q91-mCherry in DA1 ORNs and HTT_{ex1}Q25-GFP in (***A***) mz0709+ ensheathing glia or (***B***) Alrm+ astrocytic glia. Scale bars = 5 µm. ***C,D***, Quantification of (***C***) HTT_{ex1}Q91-mCherry ("mHTT") and (***D***) seeded HTT_{ex1}Q25-GFP ("mHTT+wtHTT") aggregates from flies shown in (***A,B***). Data are shown as mean ± SEM; ***$p < 0.001$ by unpaired two-tailed *t* test.

rabconnectin-3A (Y. Yan et al., 2009), and Spinster, a late-endosomal and lysosomal efflux permease (Rong et al., 2011), increased numbers of glial $wtHTT_{ex1}$ aggregates, which were detected as GFP+ surfaces that colocalized with $mHTT_{ex1}$ aggregates (Fig. 13*A–C*; Donnelly et al., 2020). Knockdown of Vha16-1, a V-ATPase subunit that regulates endolysosome membrane fusion (Finbow et al., 1994; Dunlop et al., 1995), did not affect $wtHTT_{ex1}$ seeding; however, it did cause accumulation of $mHTT_{ex1}$ aggregates in DA1 ORN axons (Fig. 13*A,B*). Together, these findings suggest that disruption of normal glial lysosome acidification and/or degradative capacity promotes formation of seeding-competent $mHTT_{ex1}$ aggregates.

The GTPase Rab10 mediates prion-like transmission of mHTT aggregates

Lysosome dysfunction could occur secondary to upstream defects in endo/phagosome maturation. Our prior work supports a model in which a portion of $mHTT_{ex1}$ aggregates engulfed by glia evade degradation during phagosome maturation and/or phagolysosome formation (Pearce et al., 2015; Donnelly et al., 2020). To test this model, we used forward genetic screening to interrogate roles for glial Rab GTPases in prion-like conversion of cytoplasmic $wtHTT_{ex1}$ proteins by engulfed neuronal $mHTT_{ex1}$ aggregates. The *Drosophila* genome encodes 31 Rab and Rab-like proteins, all of which have mammalian orthologs, and most of these GTPases are implicated in vesicle and target membrane fusion in cells (Zhang et al., 2007). To determine whether any *Drosophila* Rabs mediate escape of phagocytosed $mHTT_{ex1}$ aggregates and seeding of $wtHTT_{ex1}$ in the glial cytoplasm, we individually knocked down each *Drosophila* Rab in Repo+ glia using RNAi. Glial-restricted silencing of 23 out of 31 Rabs produced viable adults, and these flies were used to monitor effects of Rab knockdown on $mHTT_{ex1}$-induced aggregation of $wtHTT_{ex1}$ in glia. Only two Rab RNAi lines, $Rab10^{RNAi}$ and $Rab23^{RNAi\#2}$, significantly altered numbers of induced $wtHTT_{ex1}$ aggregates (Fig. 14*A–C*). Of note, 3 additional Rab23 RNAi lines had no significant effects on numbers of seeded $wtHTT_{ex1}$ aggregates, suggesting that $Rab23^{RNAi\#2}$ may cause off-target effects. Strikingly, Rab10 depletion reduced numbers of seeded $wtHTT_{ex1}$ aggregates, phenocopying effects of Draper knockdown (Fig. 14*A,C*) and suggesting that Draper and Rab10 function in the same pathway. To test whether this effect of Rab10 loss-of-function was mediated via a reduction in Draper expression, we measured endogenous Draper immunofluorescence in *rab10* null flies. Draper protein levels were ~18% lower in $rab10^{-/-}$ animals compared to wild-type controls (Fig. 14*D*). This reduction is unlikely to fully account for decreased seeding of $wtHTT_{ex1}$ following Rab10 knockdown, as numbers of $wtHTT_{ex1}$ aggregates are similar between wild-type and *draper* heterozygotes (Fig. 14*G*; Pearce et al., 2015). To further explore this, we attempted to restore Draper function via overexpression of Draper-I, which rescues loss of Draper function in aged flies (Purice et al., 2016). However, transgenic expression of Draper-I in glia failed to rescue the effects of Rab10 knockdown on $wtHTT_{ex1}$ aggregate seeding (Fig. 14*E*). These findings suggest that Rab10 acts downstream of Draper rather than by regulating Draper activity. We further tested for interactions between *drpr* and *rab10* using loss-of-function alleles to examine effects on $mHTT_{ex1}$ aggregate transmission from presynaptic DA1 ORNs to postsynaptic projection neurons (PNs), a process previously reported to require transport though Draper+ glia (Donnelly et al., 2020). Because reduced survival of *rab10* null flies (Kohrs et al., 2021) was exacerbated by transgenic HTT_{ex1} expression, we tested for genetic interaction between *drpr* and *rab10* in heterozygous and trans-heterozygous animals. While we detected no change in $mHTT_{ex1}$ aggregate numbers (Fig. 14*F*), significantly fewer $wtHTT_{ex1}$ aggregates formed in PNs of $rab10^{+/-}$ $drpr^{+/-}$ transheterozygotes than in individual heterozygotes (Fig. 14*G*). This same effect was not observed in $rab14^{+/-}$ $drpr^{+/-}$ transheterozygous animals (Fig. 14*G*), indicating that the genetic interaction is specific to *drpr* and *rab10*. Thus, Draper and Rab10 appear to function in the same phagocytic pathway that regulates prion-like transmission of phagocytosed $mHTT_{ex1}$ aggregates in the fly brain.

Neuronal mHTT aggregates alter numbers of early and late glial phagosomes

Our forward genetic screen indicates that at least one glial Rab GTPase, Rab10, regulates the seeding capacity of neuronal $mHTT_{ex1}$ aggregates. Interestingly, Rab10 has been reported to regulate phagosome maturation in mammalian cells (Cardoso et al., 2010; Seto et al., 2011; H. Lee et al., 2020; Y. Wang et al., 2023), and Rab10 expression and activity are altered in neurodegenerative diseases, including AD and PD (Eguchi et al., 2018; T. Yan et al., 2018; Tavana et al., 2018). Because little is known about Rab10's role in glia, we sought to characterize this GTPase alongside two additional Rabs with well-established roles in endocytosis, Rab5 and Rab7,

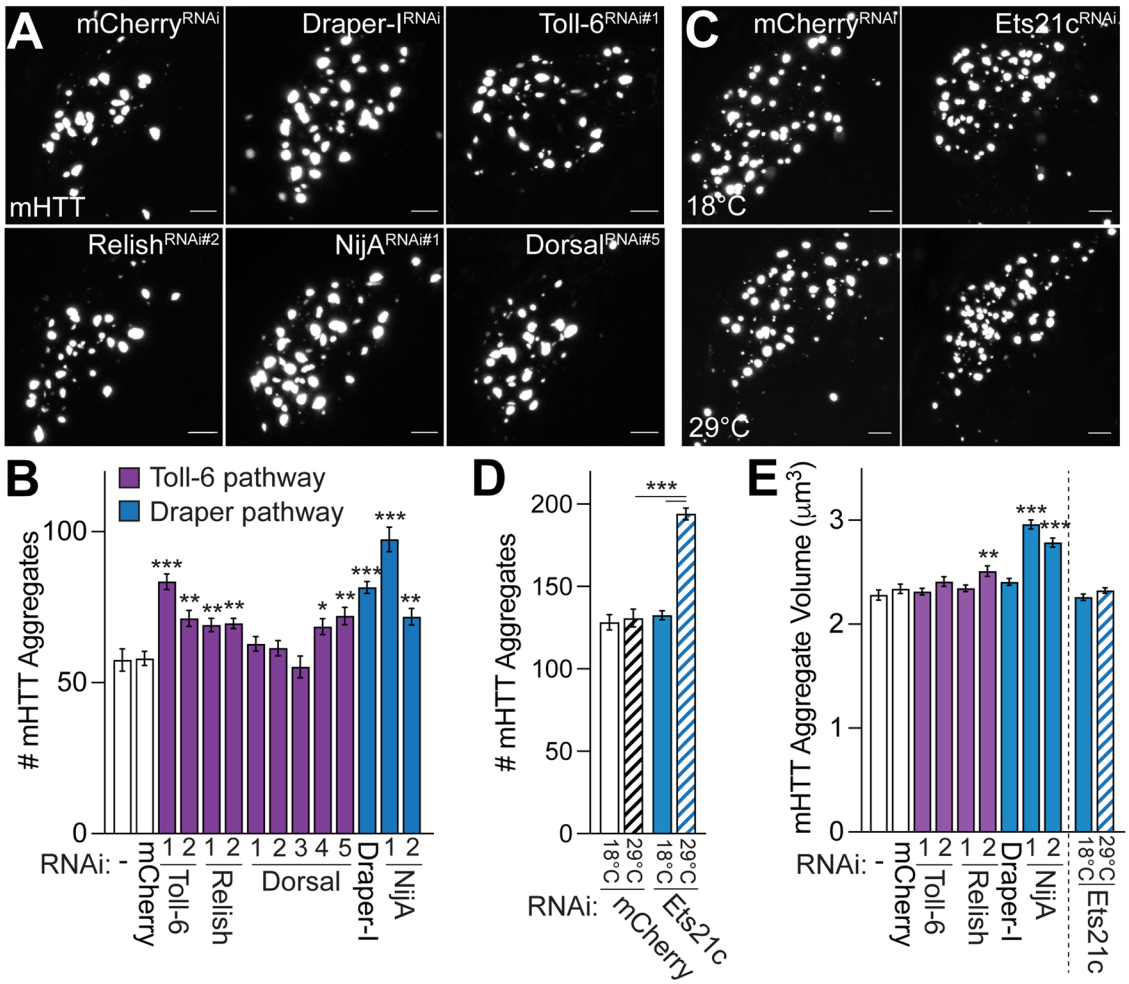

Figure 9. Glial phagocytic and innate immunity genes regulate numbers of $mHTT_{ex1}$ aggregates in ORN axons. ***A***, Maximum intensity projections of DA1 glomeruli from 7-day-old flies expressing HTT_{ex1}Q91-mCherry in DA1 ORNs and siRNAs targeting the indicated genes in ensheathing glia. Scale bars = 5 µm. ***B***, Quantification of HTT_{ex1}Q91-mCherry aggregates detected in DA1 glomeruli from flies shown in (***A***). ***C***, Maximum intensity projections of DA1 glomeruli from 7-day-old flies expressing HTT_{ex1}Q91-mCherry in DA1 ORNs and siRNAs targeting mCherry or Ets21c in repo+ glia in the presence of tubP-Gal80^{ts}. Adult flies were raised at the permissive (18°C, *top*) or restrictive (29°C, *bottom*) temperatures to restrict siRNA expression to adults. Scale bars = 5 µm. ***D***, Quantification of HTT_{ex1}Q91-mCherry aggregates detected in DA1 glomeruli from flies shown in (***C***). ***E***, Mean volumes of HTT_{ex1}Q91-mCherry aggregates detected in DA1 glomeruli from flies shown in (***A,C***). All graphed data are shown as mean ± SEM; *$p < 0.05$, **$p < 0.01$, ***$p < 0.001$ by one-way ANOVA or unpaired two-tailed *t* test compared to no RNAi or $mCherry^{RNAi}$ controls.

markers of early and late endo/phagosomes, respectively (Hutagalung and Novick, 2011). Interestingly, we found that *rab10*, *rab5*, and *rab7* were upregulated between ~1.4 and 2.4-fold following acute injury to ORN axons, and $mHTT_{ex1}$ expression in Or83b+ ORNs alone caused upregulation of *rab10* and *rab7* genes by ~1.2-fold (Fig. 15*A*). Interestingly, injury-induced upregulation of *rab5* and *rab7* was inhibited by ~50 and ~100%, respectively, in flies expressing $mHTT_{ex1}$ compared to controls (Fig. 15*A*). Altogether, these results identify *rab5*, *rab7*, and *rab10* as novel injury-response genes in the fly CNS and suggest that neuronal $mHTT_{ex1}$ aggregates impair injury-induced responses of *rab5* and *rab7*.

We next examined effects of neuronal $mHTT_{ex1}$ expression on the localization of Rab10, Rab5, and Rab7 proteins endogenously tagged with YFP-myc at their N-termini, herein referred to as YRab10, YRab5, and YRab7 (Dunst et al., 2015). YRab+ vesicles were identified in confocal stacks as segmented YFP+ surfaces with a mean diameter of 0.3–8 µm (Fig. 15*B–G*), consistent with vesicle sizes reported in other fly tissues (Prince et al., 2019). Expression of $mHTT_{ex1}$ in Or83b+ ORN axons caused an overall increase in numbers of YRab10+ and YRab7+ vesicles, but a decrease in the number of YRab5+ vesicles compared with $wtHTT_{ex1}$ controls (Fig. 15*H*). Further, each of these YRab+ vesicle subpopulations were closely associated with $mHTT_{ex1}$ aggregates more frequently than with $wtHTT_{ex1}$ (Fig. 15*I*), suggesting that $mHTT_{ex1}$ proteins interact with each of these intracellular vesicle subpopulations in the brain.

To assess effects of neuronal $mHTT_{ex1}$ aggregates specifically on glial Rab+ compartments, we expressed YFP-tagged Rab5, 7, and 10 transgenes in all glia. Similar to our findings with endogenous YRabs, expression of $mHTT_{ex1}$ in Or83b+ ORN axons was associated with increased numbers of glial YFP-Rab10+ and -Rab7+ vesicles (Fig. 16*A,B,E,F,G*); however, we observed a significant decrease in glial YFP-Rab5+ vesicle abundance (Fig. 16*C,D,G*). YFP-Rab10+, −5+, and −7+ vesicles increased their association with axonal $mHTT_{ex1}$ aggregates compared with $wtHTT_{ex1}$ (Fig. 16*H*), in many cases with closely associated YFP-Rab+ signal partially surrounding a $mHTT_{ex1}$ aggregate (Fig. 17). Of note, only a small fraction of YFP-Rab+ vesicles were identified as associated with $mHTT_{ex1}$ aggregates, possibly

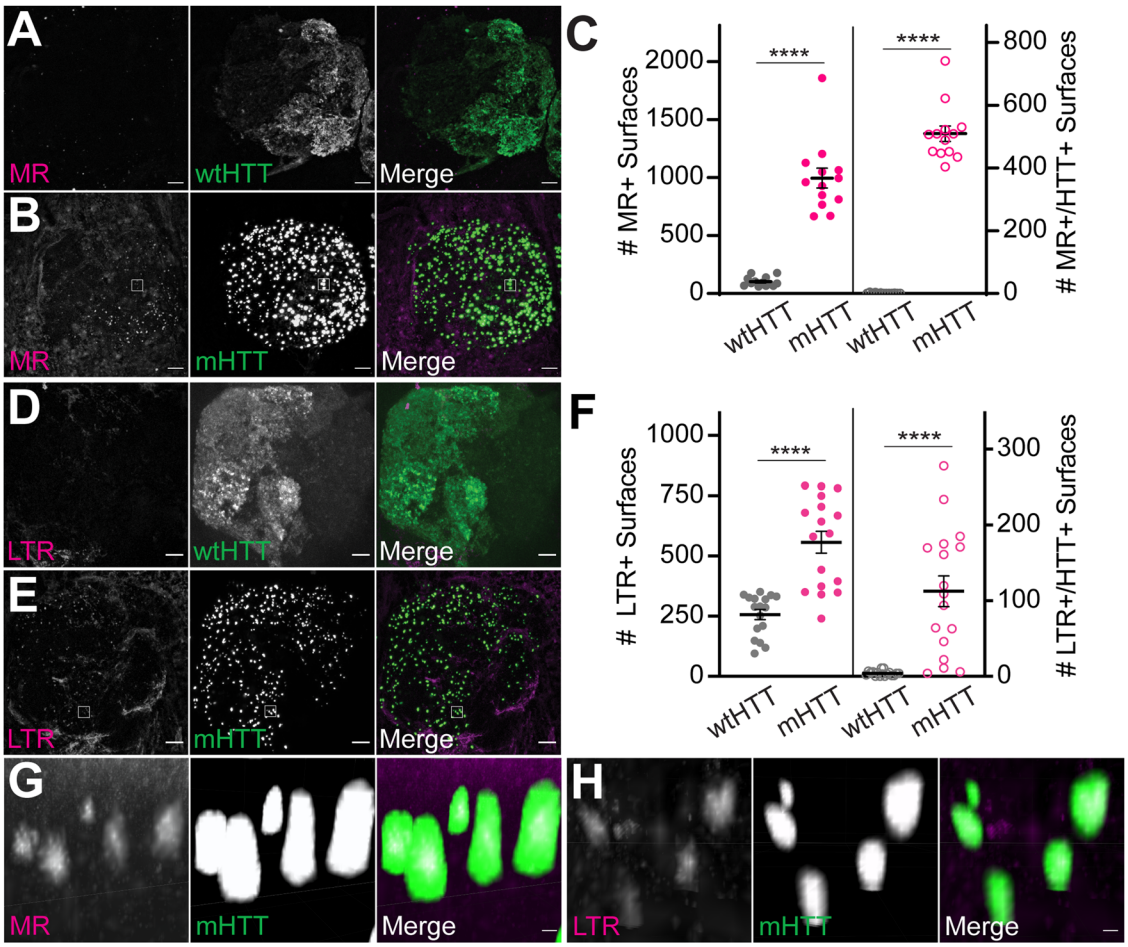

Figure 10. Neuronal $mHTT_{ex1}$ expression increases numbers of acidified and active lysosomes in adult brains. ***A,B***, Maximum intensity projections of antennal lobes from 9- to 10-day-old adult flies expressing (***A***) $HTT_{ex1}Q25$- or (***B***) $HTT_{ex1}Q91$-GFP in Or83b+ ORNs and stained with Magic Red (MR) to label active cathepsins. Scale bars = 10 µm. ***C***, Quantification of MR+ surfaces (*left*) and HTT_{ex1}-associated MR+ surfaces (*right*) from flies shown in (***A,B***); HTT_{ex1}-associated vesicles were defined by filtering for MR+ surfaces ≤0.2 µm from HTT_{ex1} fluorescent signal in confocal stacks. ***D,E***, Maximum intensity projections of antennal lobes from 15-day-old flies expressing (***D***) $HTT_{ex1}Q25$- or (***E***) $HTT_{ex1}Q91$-GFP in Or83b+ ORNs and stained with Lysotracker Red (LTR) to label low pH compartments. Scale bars = 10 µm. Diffuse $wtHTT_{ex1}$ signal was adjusted postacquisition for increased visibility in panels (***A,D***). ***F***, Quantification of LTR+ surfaces (*left*) and HTT_{ex1}-associated LTR+ surfaces (*right*) from flies shown in (***D,E***); HTT_{ex1}-associated vesicles were defined by filtering for LTR+ surfaces ≤0.2 µm from HTT_{ex1} fluorescent signal in confocal stacks. Data are shown as mean ± SEM; ****$p < 0.0001$ by unpaired two-tailed *t* test. ***G,H***, High-magnification regions of interest indicated in (***B,E***) showing colocalization of MR (***G***) or LTR (***H***) with $mHTT_{ex1}$ fluorescent signals. Scale bars = 1 µm.

due to transient interactions with vesicle compartments as aggregates transit the glial phagolysosomal system, heterogeneous labeling of phagosomes by these markers in intact brain tissue, or because our selection filter excluded YFP-Rab+ surfaces located >0.2 µm away from an aggregate. The mean volume of YFP-Rab7+ vesicles that interacted with $mHTT_{ex1}$ aggregates was significantly increased compared with $wtHTT_{ex1}$ controls (Fig. 16*I*), suggesting that $mHTT_{ex1}$ leads to enlargement of Rab7+ late phagolysosomes. Together, these data suggest that accumulation of phagocytosed $mHTT_{ex1}$ aggregates in Rab7+ or Rab10+ late phagosomes and decreased association with early Rab5+ phagosomes could be a key mechanism underlying protein aggregate-induced toxicity and spreading in HD.

Discussion

Toxic amyloid aggregates have been a primary target in neurodegenerative disease drug development for decades, with some recent promise using immunotherapy to reduce aggregate loads in the brain (Karran and De Strooper, 2022). Microglia and astrocytes have also emerged as attractive therapeutic targets in efforts to boost neuroprotective glial functions or reduce neuroinflammation. However, approaches that target glial cells must effectively strike a balance between amplifying beneficial and reducing harmful effects of these cells in the brain. Here, we tested for interactions between phagocytic glia and pathogenic protein aggregates in a *Drosophila* model of HD. We report that aggregates formed by $mHTT_{ex1}$ protein fragments impair glial transcriptional and functional responses to CNS injury, induce upregulation of stress response and innate immunity genes, and alter numbers of endolysosomal vesicles detected in uninjured brains. A targeted forward genetic screen revealed that Rab10, a GTPase previously reported to regulate phagosome maturation, mediates prion-like conversion of cytoplasmic $wtHTT_{ex1}$ proteins by phagocytosed $mHTT_{ex1}$ aggregates. Together, these findings suggest that neuronal $mHTT_{ex1}$ aggregates compromise intracellular membrane integrity as they transit endolysosomal systems, generating toxic, seeding-competent aggregates that propagate disease phenotypes.

Glia respond to neural injury by altering their transcriptional, morphological, and metabolic profiles to promote neuronal survival and clear debris from the brain; however, failure of

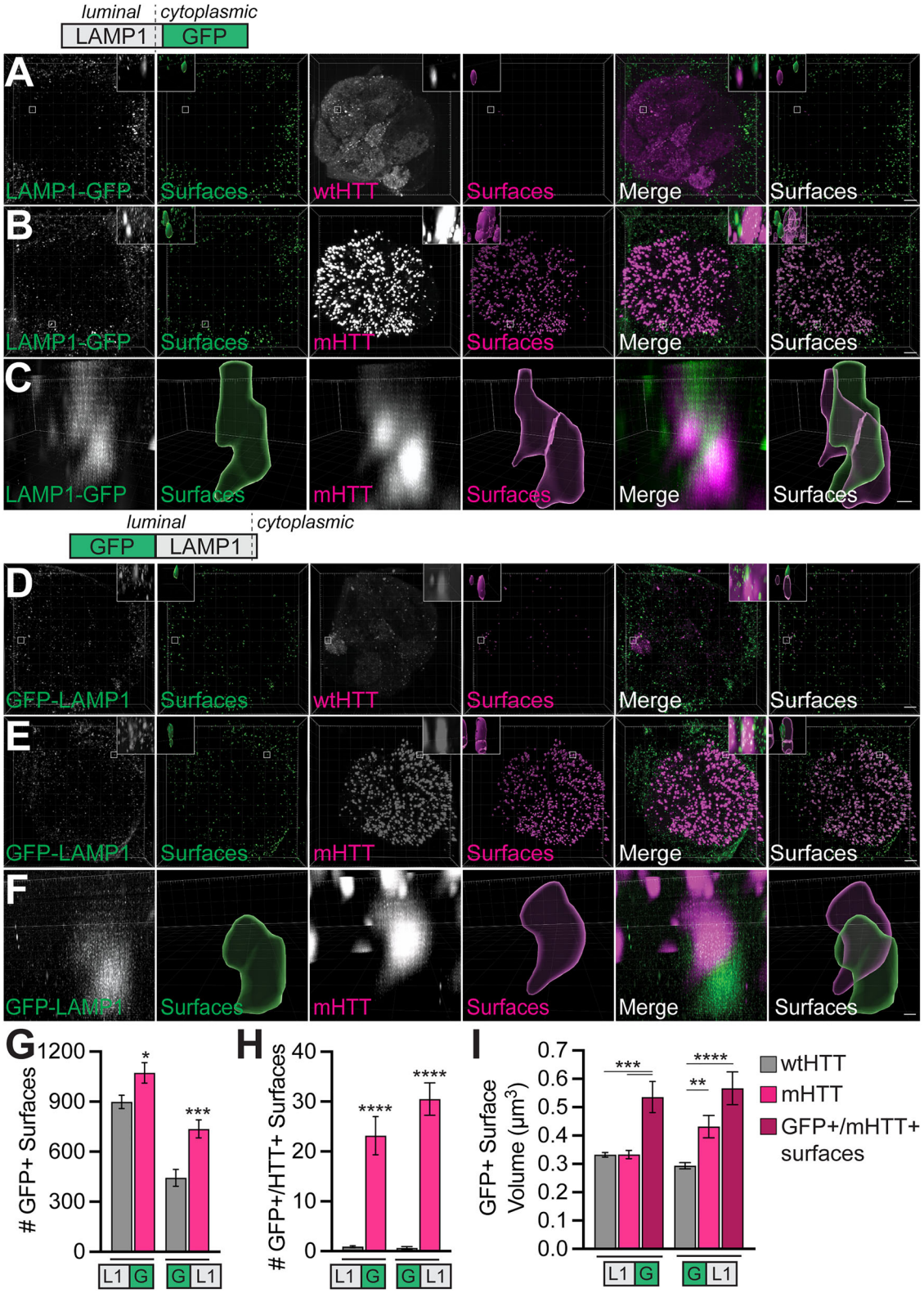

Figure 11. LAMP1+ vesicle accumulation in fly brains expressing $mHTT_{ex1}$ in ORNs. ***A,B***, Confocal stacks showing antennal lobes from 19- to 22-day-old flies expressing (***A***) HTT_{ex1}Q25- or (***B***) HTT_{ex1}Q91-mCherry in Or83b+ ORNs and LAMP1 tagged at its cytoplasmic C-terminus with GFP (LAMP1-GFP) in glia. Brains were immunostained with anti-GFP to amplify LAMP1-GFP signal. LAMP1-GFP+ or HTT_{ex1}+ segmented surfaces are shown to the right of each set of raw fluorescence images. Insets show magnified regions of interest from each image. Scale bars = 10 µm. ***C***, High-magnification confocal stack showing a LAMP1-GFP+ surface within 0.2 µm of two HTT_{ex1}Q91-mCherry+ aggregates. Scale bar = 1 µm. ***D,E***, Confocal stacks showing antennal lobes from 21- to 22-day-old flies expressing (***D***) HTT_{ex1}Q25- or (***E***) HTT_{ex1}Q91-mCherry in Or83b+ ORNs and LAMP1 tagged at its luminal N-terminus with GFP (GFP-LAMP1) in glia. GFP-LAMP1+ or HTT_{ex1}+ segmented surfaces are shown to the right of each set of raw fluorescence images. Insets show GFP-LAMP1+ surfaces of interest from each image at high magnification. Scale bars = 10 µm. Diffuse $wtHTT_{ex1}$ signal was adjusted postacquisition for increased visibility in panels (***A,D***). ***F***, High-magnification confocal stack showing a GFP-LAMP1+ surface within 0.2 µm of a HTT_{ex1}Q91-mCherry+ aggregate. Scale bar = 1 µm. ***G–I***, Quantification of total LAMP1-GFP+ or GFP-LAMP1+ surfaces (***G***), LAMP1-GFP+ or GFP-LAMP1+ surfaces ≤0.2 µm from HTT_{ex1} surfaces (***H***), and mean LAMP1-GFP+ or GFP-LAMP1+ surface volume (***I***) in brains expressing HTT_{ex1}Q25- or HTT_{ex1}Q91-mCherry. The dark red bars in (***I***) represent LAMP1+ surfaces that colocalized with $mHTT_{ex1}$. All graphed data are shown as mean ± SEM; *$p < 0.05$, **$p < 0.01$, ***$p < 0.001$, ****$p < 0.0001$ by unpaired two-tailed *t* test.

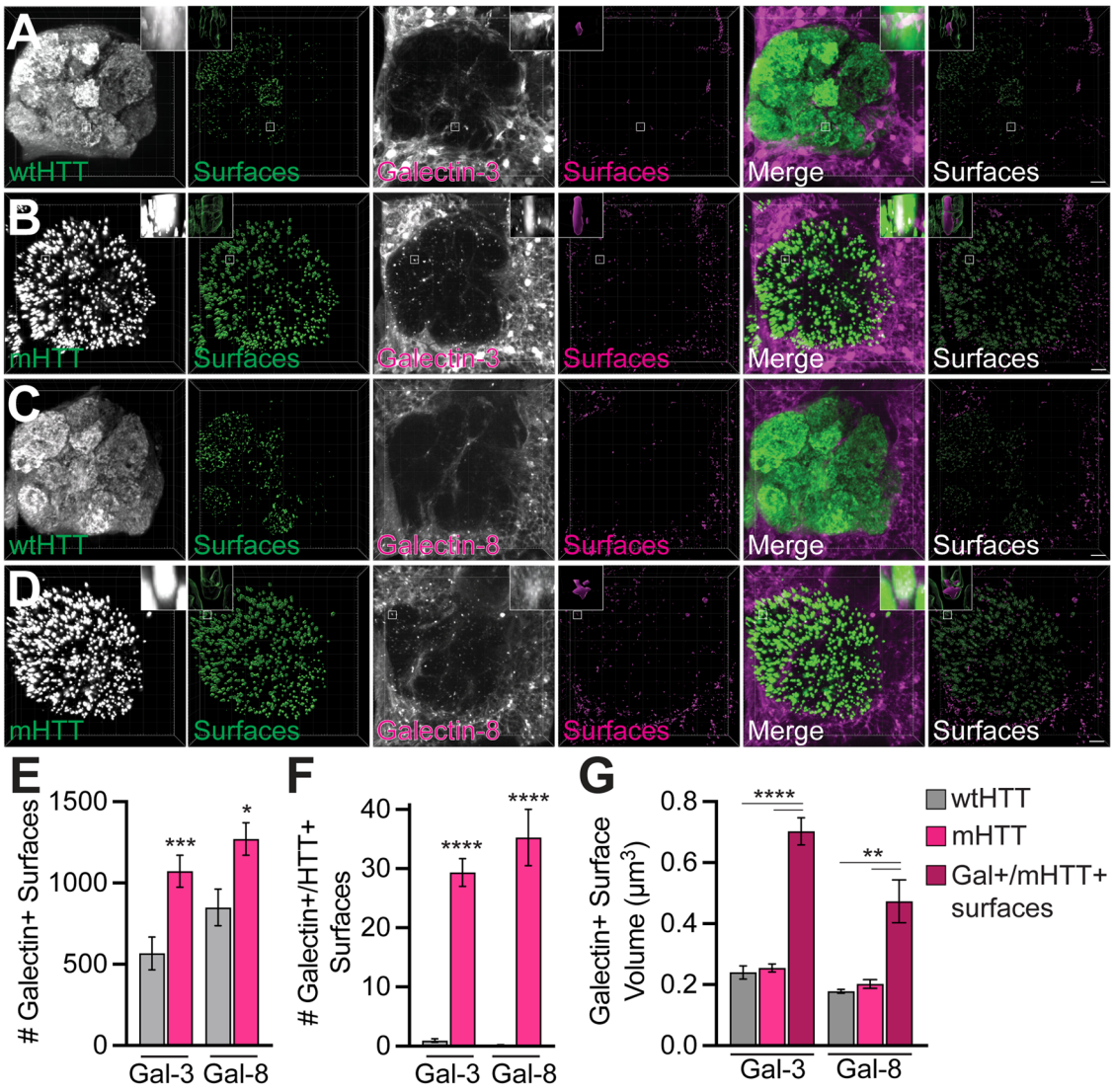

Figure 12. Increased association of glial Galectins-3 and −8 with neuronal $mHTT_{ex1}$ aggregates. ***A–D***, Confocal stacks showing antennal lobes from 16- to 18-day-old flies expressing HTT_{ex1}Q25- (***A,C***) or HTT_{ex1}Q91-GFP (***B,D***) in Or83b+ ORNs together with Galectin-3 (***A,B***) or Galectin-8 (***C,D***) tagged with mCherry in glia. Segmented Galectin+ or HTT_{ex1}+ surfaces are shown to the right of each set of raw fluorescence images. Insets show Galectin+ surfaces of interest from each image. Scale bars = 10 µm. ***E–G***, Quantification of total Galectin+ surfaces (***E***), Galectin+ surfaces ≤0.2 µm from HTT_{ex1} surfaces (***F***), and mean Galectin+ surface volume (***G***) in brains expressing HTT_{ex1}Q25- or HTT_{ex1}Q91-mCherry. The dark red bars in (***G***) represent Galectin+ surfaces that colocalized with $mHTT_{ex1}$. All graphed data are shown as mean ± SEM; $*p < 0.05$, $**p < 0.01$, $***p < 0.001$, $****p < 0.0001$ by unpaired two-tailed *t* test.

glia to return to a resting state elicits harmful neuroinflammatory consequences (Liddelow et al., 2020). We have previously reported that activated phagocytic glia can have both beneficial (i.e., elimination of toxic aggregates) and harmful (i.e., as vectors for aggregate spread) effects in the brain (Pearce et al., 2015; Donnelly et al., 2020). We report here that key glial injury-responsive pathways, i.e., Draper-mediated phagocytosis and Toll-6-mediated innate immune signaling, are induced in the presence $mHTT_{ex1}$ aggregation in the adult fly brain. These findings are in line with studies from other labs demonstrating that *Drosophila* Toll-6 and mammalian Toll-like receptor signaling pathways are upregulated in response to dying neurons during development (McLaughlin et al., 2019) and in patients and mammalian models of neurodegenerative disease (Casula et al., 2011; Miron et al., 2018; Kouli et al., 2020). Interestingly, increased microglial NF-κB signaling mediates tau spread and toxicity in mice, further linking innate immunity to prion-like mechanisms of disease progression (C. Wang et al., 2022). Thus, activation of glial immune pathways may contribute to feed-forward mechanisms involving aggregate formation, pathology propagation, and neuroinflammatory signaling.

Genome-wide association studies have revealed numerous genes associated with increased risk of AD and other neurodegenerative diseases, and many of these risk variants are enriched in pathways that control key glial cell functions. For example, rare risk-associated variants of the microglial *TREM2* gene alter amyloid aggregate accumulation and seeding in cells and animal models (Leyns et al., 2019; Parhizkar et al., 2019; Jain et al., 2023). A number of additional genes involved in endolysosomal processing are associated with increased risk of AD, PD, FTD, and/or ALS, such as the phagocytic receptor *CD33*, endosomal genes *BIN1* and *RIN3*, and *GRN*, which encodes the lysosomal progranulin protein (Podleśny-Drabiniok et al., 2020; Welikovitch et al., 2023). Although Draper/MEGF10 variants are not known risk factors in neurodegenerative disease, MEGF10 is highly expressed in

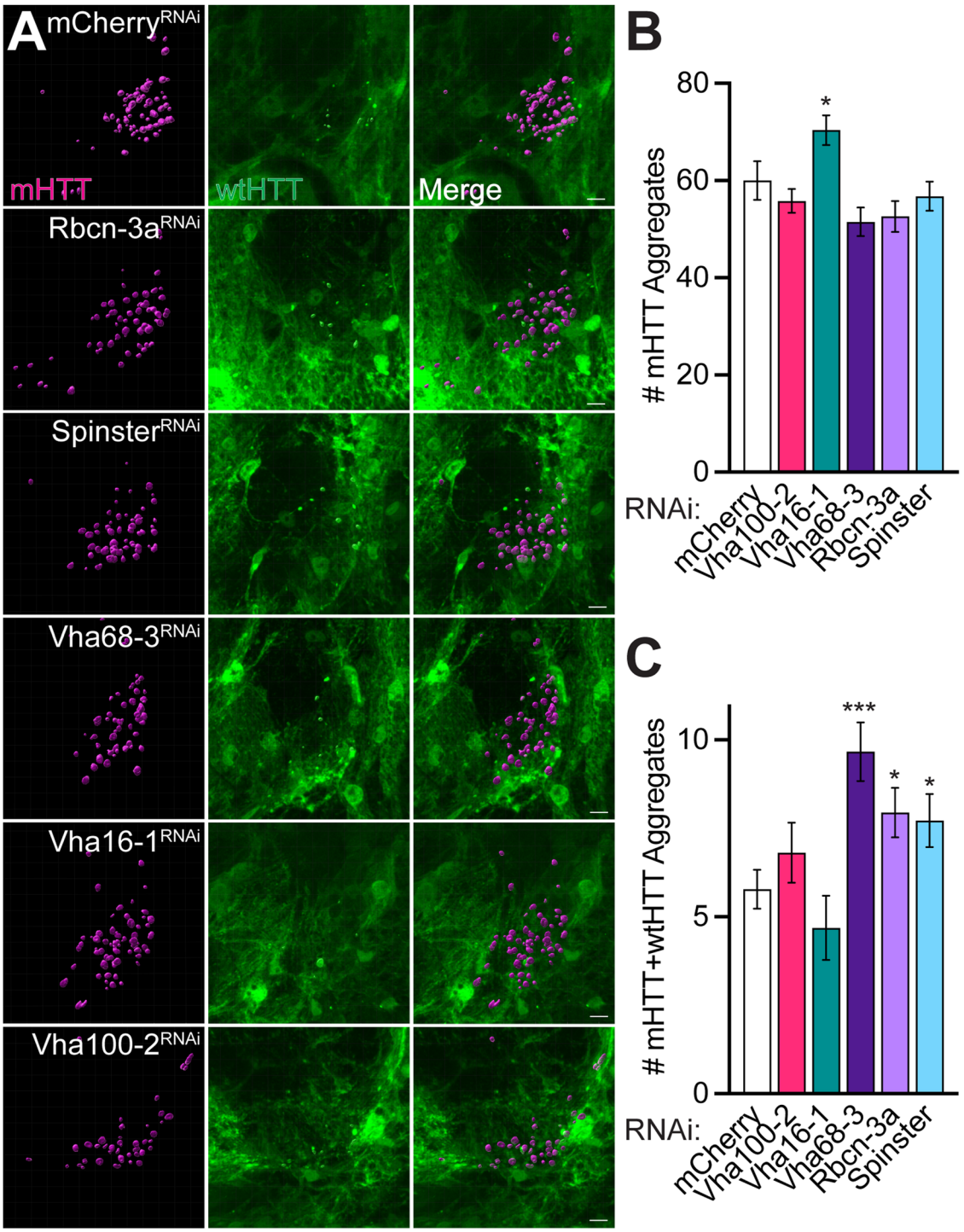

Figure 13. Knockdown of genes regulating lysosome acidification alters seeded aggregation of glial wtHTT$_{ex1}$ protein by neuronal mHTT$_{ex1}$ aggregates. ***A***, Confocal stacks showing DA1 glomeruli from 8- to 9-day-old flies expressing HTT$_{ex1}$Q91-mCherry in DA1 ORNs and HTT$_{ex1}$Q25-GFP plus siRNAs targeting the indicated genes in repo+ glia. Negative controls expressed siRNAs targeting mCherry. Scale bars = 5 µm. ***B,C***, Quantification of (***B***) HTT$_{ex1}$Q91-mCherry or (***C***) seeded HTT$_{ex1}$Q25-GFP aggregates from brains shown in (***A***). Data are shown as mean ± SEM; $*p < 0.05$, $***p < 0.005$ by unpaired two-tailed *t* test.

phagocytic astrocytes (Chung et al., 2013), mediates Aβ aggregate engulfment (Singh et al., 2010; Fujita et al., 2020), and acts as a receptor for C1q, a mediator of early synapse loss in AD mouse models (Hong et al., 2016; Iram et al., 2016). Our finding that upregulation of *draper* and other phagocytic genes is inhibited by mHTT$_{ex1}$ expression suggests that glial responsiveness and phagocytic capacity is attenuated in the presence of protein aggregates in neurons. Genetic or environmental risk factors that impact glial health could accelerate these defects and exacerbate aggregate-induced neurotoxicity in the brain.

Lysosomes are essential for cell survival, not only to clear damaged or toxic materials from cells, but also as intracellular centers for macromolecule recycling, energy metabolism, and cell-cell communication. Lysosomal abnormalities, including vesicle

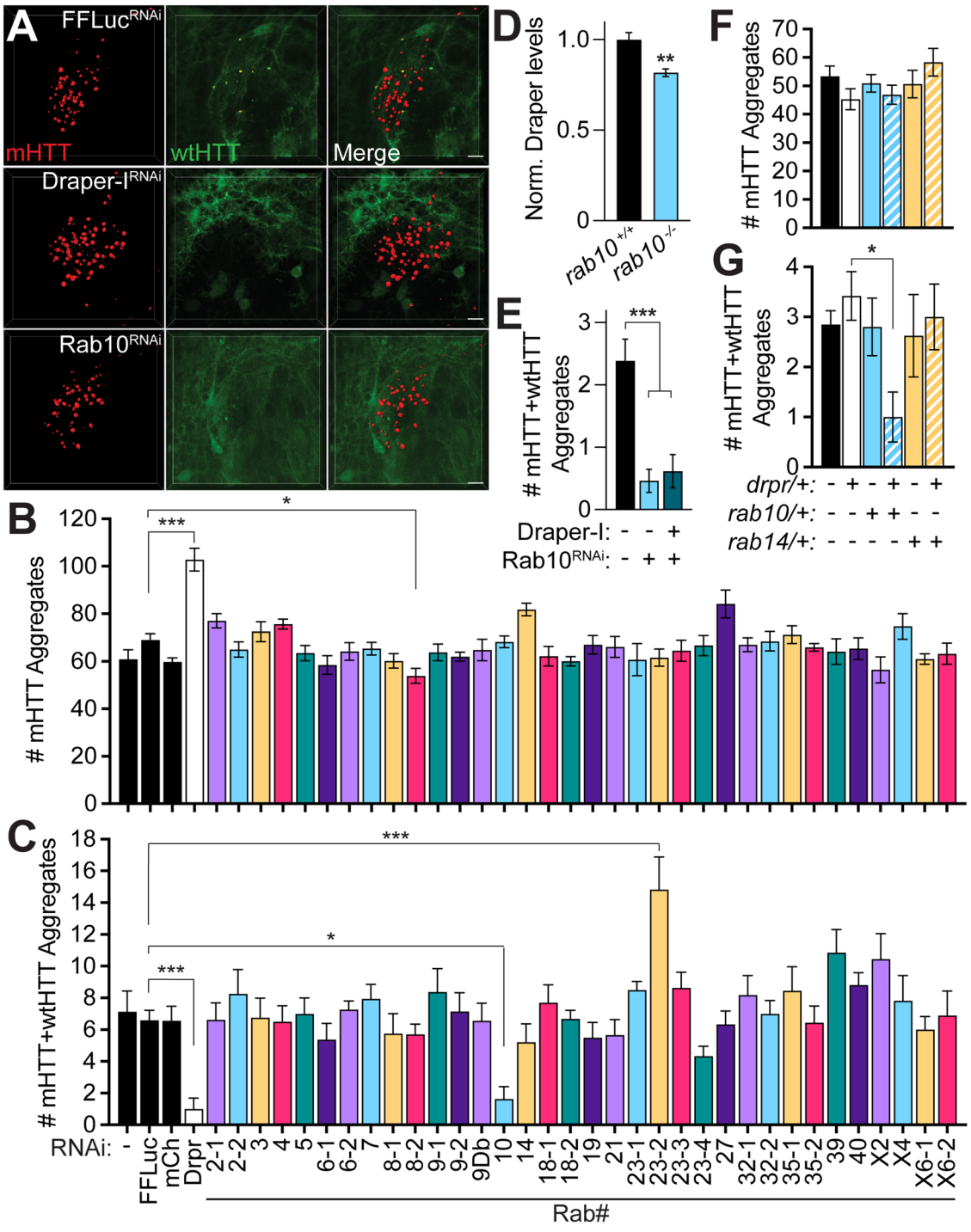

Figure 14. Rab10 is required for seeded aggregation of glial wtHTT$_{ex1}$ by neuronal mHTT$_{ex1}$ aggregates. ***A***, Confocal stacks of DA1 glomeruli from 7-day-old flies expressing HTT$_{ex1}$Q91-mCherry in DA1 ORNs and HTT$_{ex1}$Q25-GFP plus siRNAs targeting firefly luciferase (FFLuc), Draper, or Rab10 in repo+ glia. Surfaces representing mHTT$_{ex1}$ aggregates (*red*) and seeded wtHTT$_{ex1}$ aggregates (*yellow*) are superimposed on the raw data. Scale bars = 5µm. ***B,C***, mHTT$_{ex1}$ (***B***) or mHTT$_{ex1}$+wtHTT$_{ex1}$ (***C***) aggregates quantified from flies expressing HTT$_{ex1}$Q91-mCherry in DA1 ORNs and HTT$_{ex1}$Q25-GFP plus siRNAs targeting Draper-I (Drpr) or 23 different Rab GTPases in Repo+ glia. Negative controls expressed no siRNAs or siRNAs targeting FFLuc or mCherry (*black bars*). ***D***, Normalized Draper immunofluorescence in the central brain of 4- to 5-day-old wild-type (*rab10*$^{+/+}$) and *rab10* null (*rab10*$^{-/-}$) flies. ***E***, Quantification of seeded wtHTT$_{ex1}$ aggregates in flies expressing HTT$_{ex1}$Q91-mCherry in DA1 ORNs and HTT$_{ex1}$Q25-GFP plus siRNAs targeting Rab10, without or with Draper-I cDNAs in repo+glia. ***F,G***, Quantification of mHTT$_{ex1}$ (***F***) or mHTT$_{ex1}$+wtHTT$_{ex1}$ (***G***) aggregates from 10-day-old flies expressing HTT$_{ex1}$Q91-mCherry in DA1 ORNs and HTT$_{ex1}$Q25-GFP in PNs, either heterozygous or trans-heterozygous for *draper* (*drpr/+*), *rab10* (*rab10/+*), or *rab14* (*rab14/+*) mutant alleles. All graphed data are shown as mean ± SEM; *$p < 0.05$, **$p < 0.01$, ***$p < 0.005$ by one-way ANOVA or unpaired two-tailed *t* test comparing to controls.

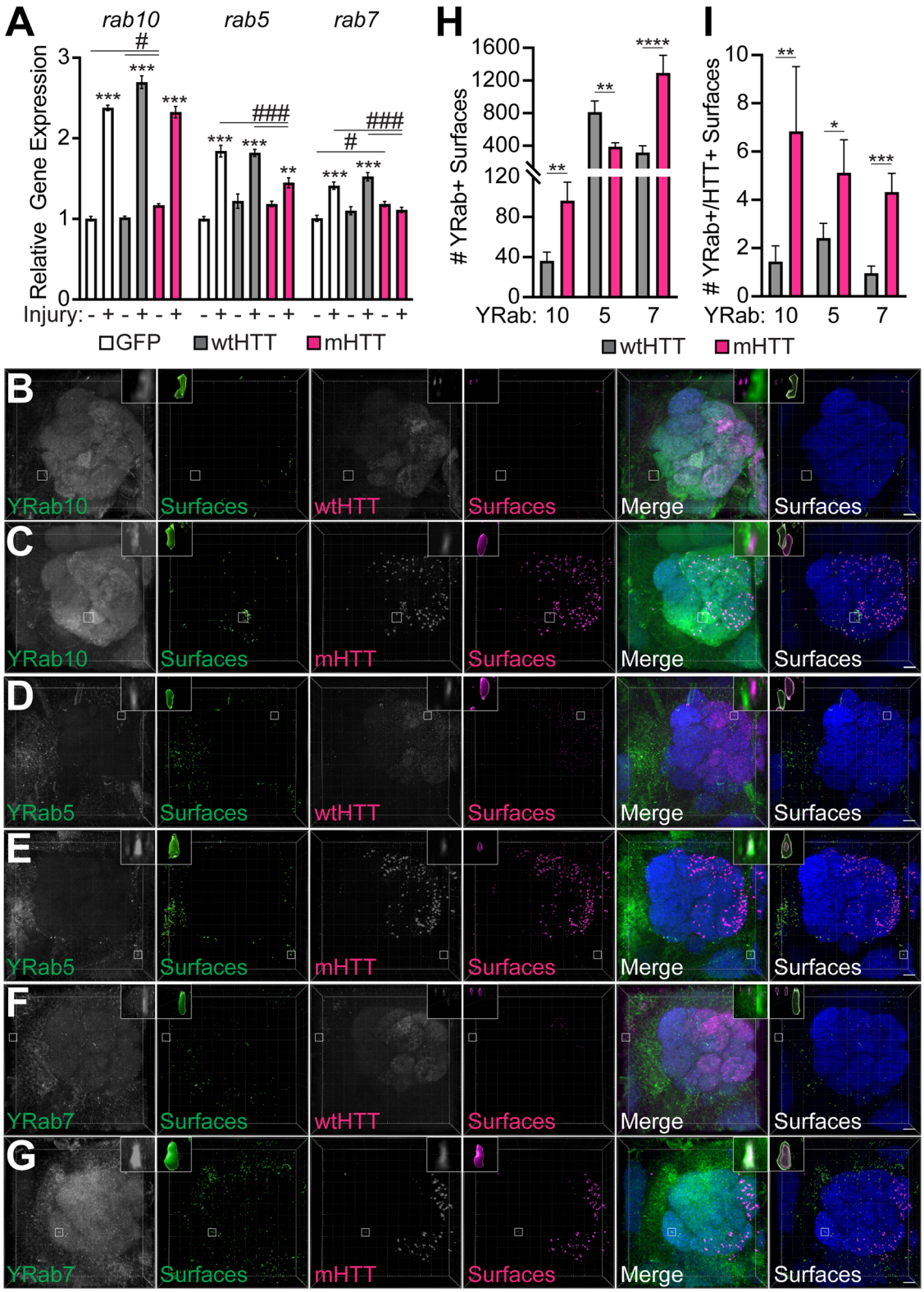

Figure 15. Association of neuronal $mHTT_{ex1}$ aggregates with Rab GTPases that associate with early, maturing, and late phagosomes. ***A***, qPCR analysis of *rab10*, *rab5*, and *rab7* expression in 8- to 11-day-old flies expressing GFP, HTT_{ex1}Q25-, or HTT_{ex1}Q91-GFP in Or83b+ ORNs. RNA was isolated from heads of uninjured flies or flies 3 h after bilateral antennal and maxillary palp nerve injury. Data are shown as mean ± SEM and normalized to the housekeeping gene *rpl32*. *$p < 0.05$, **$p < 0.01$, ***$p < 0.001$ by one-way ANOVA; asterisks and hashtags indicate statistical significance comparing ± injury or genotypes, respectively. ***B–G***, Confocal stacks of the antennal lobe from 7-day-old flies expressing (***B,D,F***) HTT_{ex1}Q25- or (***C,E,G***) HTT_{ex1}Q91-V5 in Or83b+ ORNs and endogenously-tagged (***B,C***) YRab10, (***D,E***) YRab5, or (***F,G***) YRab7 in all cells. Brains were immunostained using YFP (*green*), V5 (*magenta*), and N-Cadherin (*blue*) antibodies. Segmented YRab+ or HTT+ surfaces are shown to the right of each set of raw fluorescent images. Insets show magnified YFP+ surfaces of interest from each image. Diffuse $wtHTT_{ex1}$ signal was adjusted post-acquisition for increased visibility in panels (***B,D,F***). Scale bars = 10 µm. ***H,I***, Quantification of YRab+ surfaces (***H***) and YRab+ surfaces within 0.2µm of HTT_{ex1}+ surfaces (***I***). Data are shown as mean ± SEM; *$p < 0.05$, **$p < 0.01$, ***$p < 0.001$, ****$p < 0.0001$ by unpaired two-tailed *t* test.

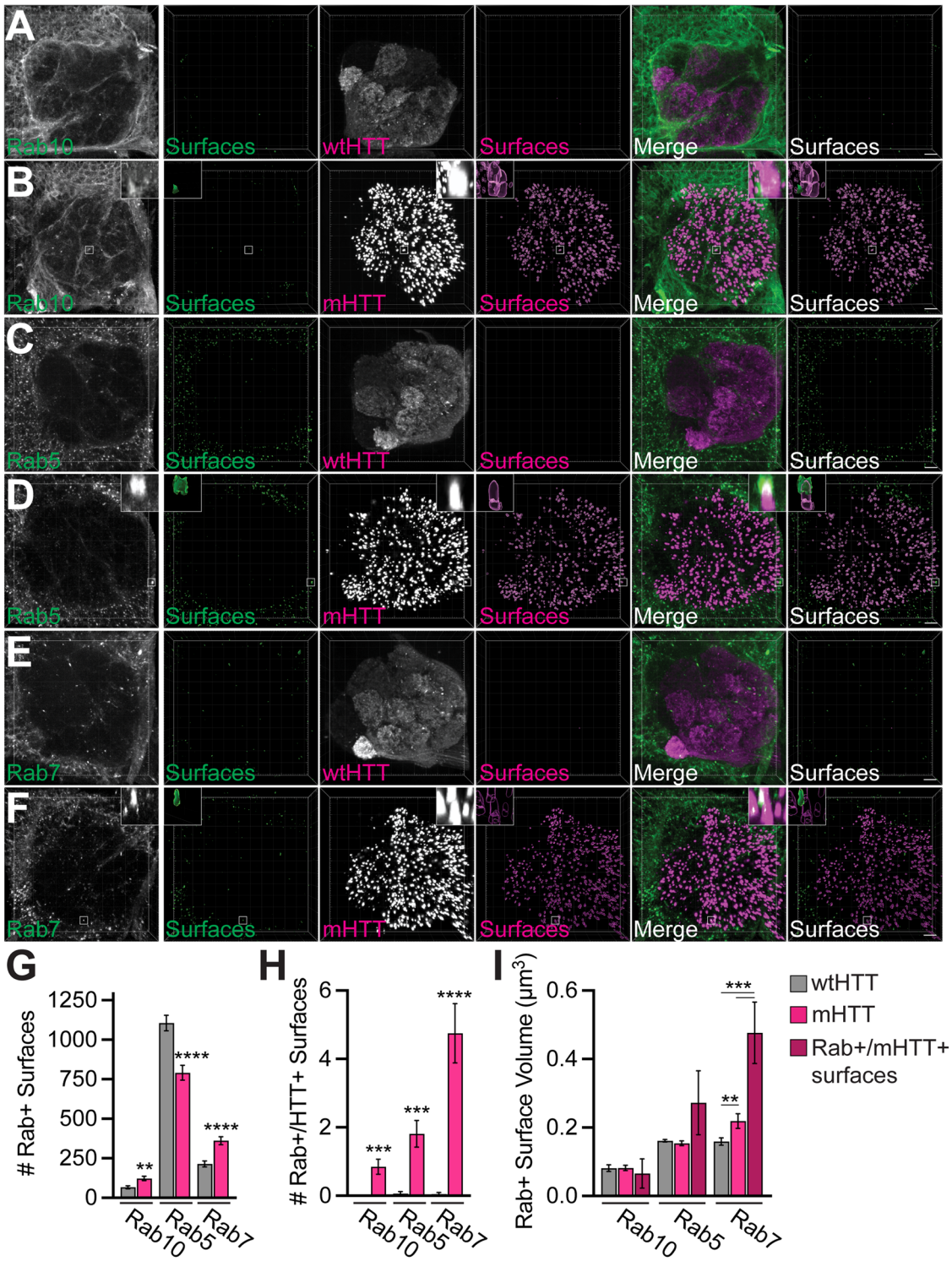

Figure 16. Association of neuronal mHTT aggregates with glial Rab GTPases that label early, maturing, and late phagosomes. ***A–F***. Confocal stacks of the antennal lobe from 16- to 19-day-old flies expressing (***A,C,E***) HTT_{ex1}Q25- or (***B,D,F***) HTT_{ex1}Q91-V5 in Or83b+ ORNs together with (***A,B***) YFP-Rab10, (***C,D***) YFP-Rab5, or (***E,F***) YFP-Rab7 in repo+ glia. Brains were immunostained with anti-GFP to amplify YFP-Rab signals. Segmented Rab+ or HTT_{ex1}+ surfaces are shown to the right of each set of raw fluorescence images. Insets show magnified YFP-Rab+ surfaces of interest from each image. Diffuse $wtHTT_{ex1}$ signal was adjusted postacquisition for increased visibility in panels (***A,C,E***). Scale bars = 10 µm. ***G–I***, Quantification of total YFP-Rab+ surfaces (***G***), YFP-Rab + surfaces ≤0.2 µm from HTT_{ex1} surfaces (***H***), and mean YFP-Rab+ surface volume (***I***) in brains expressing HTT_{ex1}Q25- or HTT_{ex1}Q91-mCherry. The dark red bars in (***I***) represent YFP-Rab+ surfaces that colocalized with $mHTT_{ex1}$. All graphed data are shown as mean ± SEM; $*p < 0.05$, $**p < 0.01$, $***p < 0.001$, $****p < 0.0001$ by unpaired two-tailed *t* test.

enlargement, deacidification, and membrane leakiness, have been reported in patient brains and animal and cell models of multiple neurodegenerative diseases, suggesting that these defects play a central role in disease progression (Bonam et al., 2019; Polanco and Götz, 2022; Udayar et al., 2022). We report here that Rab7+, Rab10+, and Lamp1+ phagolysosomes accumulate in glia as a result of $mHTT_{ex1}$ expression in neurons and that lysosome dysfunction and membrane permeabilization increase in the presence

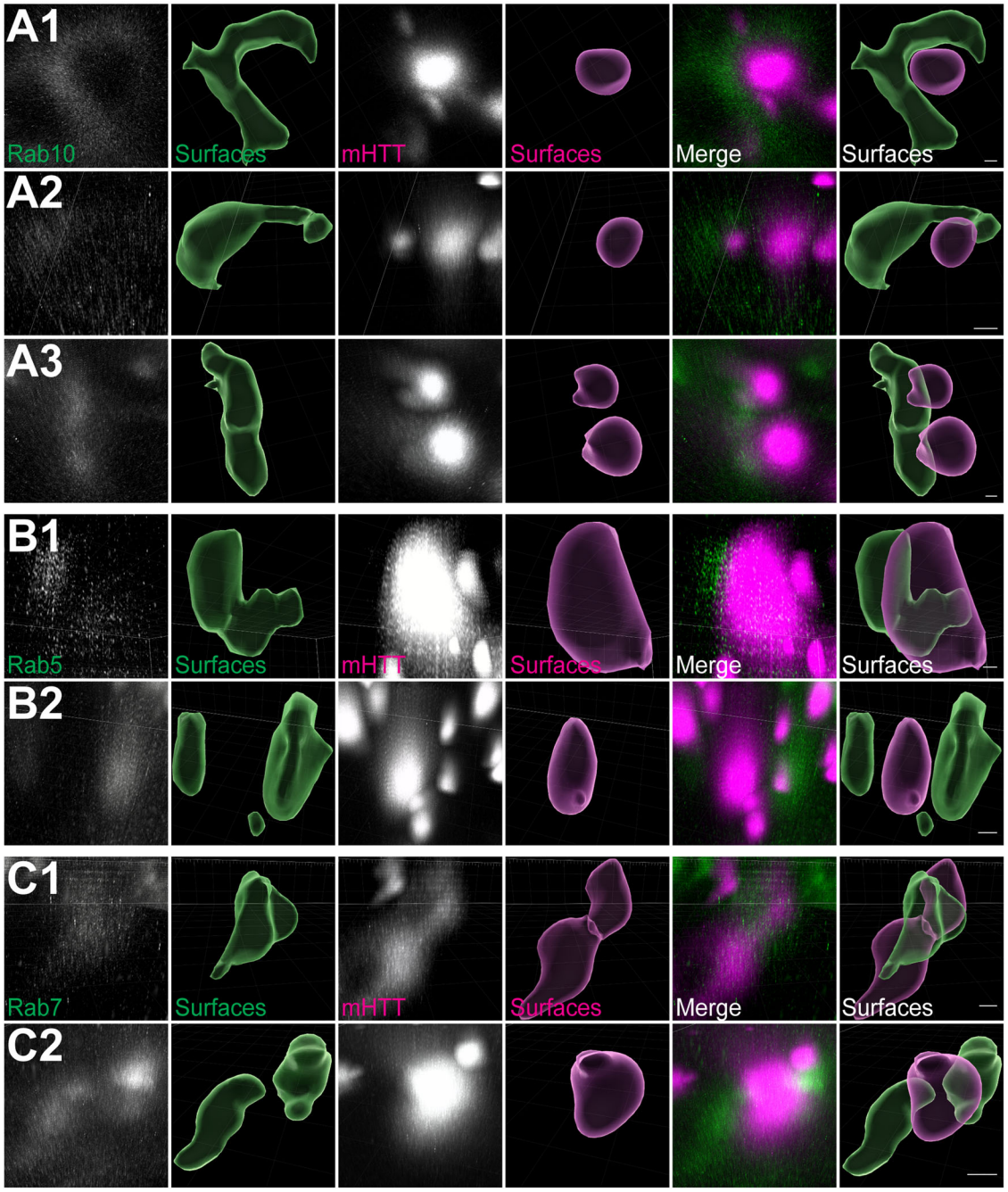

Figure 17. Glial YFP-Rab+ surfaces closely associate with neuronal mHTT$_{ex1}$ aggregates. High magnification confocal stacks showing examples of individual YFP+ surfaces within 0.2 µm of HTT$_{ex1}$Q91 aggregates from 21- to 22-day-old adult brains expressing HTT$_{ex1}$Q91-mCherry in Or83b+ ORNs and YFP-Rab10 (***A1–3***), YFP-Rab5 (***B1,2***), or YFP-Rab7 (***C1,2***) in repo+ glia. Brains were immunostained with anti-GFP to amplify YFP-Rab signals. Scale bars = 1 µm.

of mHTT$_{ex1}$ aggregates. We also observed that neuronal aggregates were associated with decreased nascent phagosome formation and reduced numbers of early (Rab5+) phagosomes in glia. These findings are consistent with a "traffic jam" model (Small et al., 2017) in which mHTT$_{ex1}$ aggregates accumulate over time in glial endolysosomal compartments, preventing proper flow of materials into (i.e., engulfment) and out of (i.e., degradation) the pathway (Fig. 18). We postulate that persistence of aggregates in faulty endolysosomes promotes formation and/or release of degradation-resistant aggregates with enhanced toxicity and seeding capacity. This hypothesis is in agreement with recent studies in tauopathy models showing that Aβ aggregation occurs secondary to lysosome deacidification and membrane permeabilization (J-H. Lee et al., 2022), and hypophagocytic glia contribute to tau aggregate propagation (Hopp et al., 2018; Brelstaff et al., 2021). Release of seeding-competent aggregates from dysfunctional lysosomes could occur via active exocytosis, perhaps in an effort to alleviate cell toxicity, or passively due to vesicle rupture (Flavin et al., 2017; Falcon et al., 2018; Yuste-Checa et al., 2021).

Among the growing list of genes linked to neurodegenerative disease pathogenesis are Rab GTPases and genes that modify Rab functions (Kiral et al., 2018). Rab proteins are essential for vesicle sorting and trafficking in all cells and use GTP hydrolysis to differentially associate with and organize intracellular

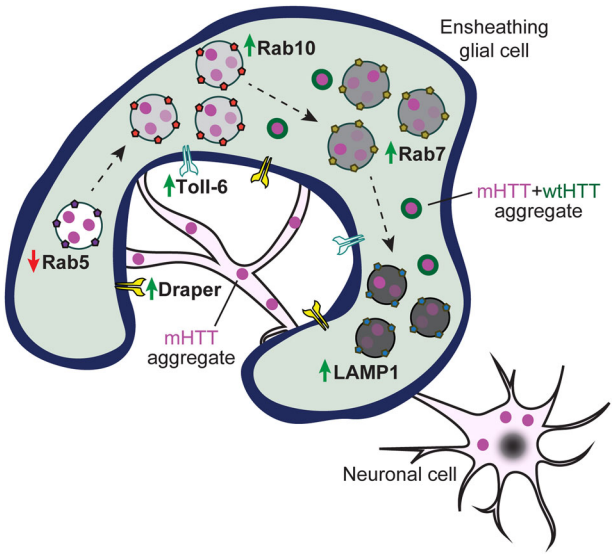

Figure 18. "Traffic jam" model illustrating effects of neuronal $mHTT_{ex1}$ aggregates on phagocytic glia. $mHTT_{ex1}$ aggregates (magenta circles) generated in axons cause phagolysosomal defects in nearby glial cells. Neuronal $mHTT_{ex1}$ aggregates activate glial Draper and Toll-6 signaling pathways (green arrows), but impair normal phagocytic responses to injury, including reduced nascent phagosome formation and decreased numbers of Rab5+ early phagosomes (red arrow). A buildup of engulfed $mHTT_{ex1}$ aggregates in glia leads to accumulation of maturing (Rab10+ or Rab7+) phagosomes and lysosomes (LAMP1+) (green arrows), possibly further slowing Draper-dependent engulfment and early phagosome formation. Defective phagocytic clearance could enhance leak or release of some $mHTT_{ex1}$ aggregates from phagolysosomes to increase their toxicity and capacity to seed soluble HTT proteins (magenta + green circles).

membranes (Homma et al., 2021). In a forward genetic screen aimed at identifying Rabs that regulate phagocytic processing of neuronal $mHTT_{ex1}$ aggregates, we uncovered glial Rab10 as a modifier of prion-like spreading of $mHTT_{ex1}$ from neurons to glia. Interestingly, several Rab proteins have been previously reported to alter secretion or cell-to-cell propagation of tau or α-synuclein aggregates (Rodriguez et al., 2017; Bae et al., 2018; Ugbode et al., 2019; Rodrigues et al., 2022), suggesting that Rab-dependent endomembrane fusion could be exploited by prion-like aggregates. Our data suggest that Rab10 acts downstream of Draper to enable engulfed $mHTT_{ex1}$ aggregates to evade lysosomal degradation, perhaps escaping to the cytoplasm during Rab10-dependent vesicle fusion. While relatively understudied compared with other Rabs, Rab10 has been reported to localize to and regulate maturing endo/phagosomes and lysosomes in human macrophages and microglia (Cardoso et al., 2010; H. Lee et al., 2020). Interestingly, Rab10 has already been implicated in multiple neurodegenerative diseases: (1) *RAB10* gene expression is altered in human AD brains (Ridge et al., 2017), (2) rare *RAB10* polymorphisms are linked to protection against AD (Ridge et al., 2017; Tavana et al., 2018), (3) Rab10 depletion is associated with reduced Aβ levels (Udayar et al., 2013; Ridge et al., 2017), and (4) Rab10 is a substrate of the PD risk factor gene LRRK2 (Steger et al., 2016; Seol et al., 2019). Mutant LRRK2-mediated Rab phosphorylation leads to endocytic defects (Rivero-Ríos et al., 2020; Z. Liu et al., 2020; Streubel-Gallasch et al., 2021), and LRRK2-modified Rab10 localizes to and promotes secretion from stressed lysosomes (Eguchi et al., 2018; Kluss et al., 2022). Interestingly, phosphorylated Rab10 (pRab10) levels are elevated in the CNS of AD and PD patients, and pRab10 has been reported to colocalize with pathological tau (T. Yan et al., 2018; Tezuka et al., 2022), suggesting that post-translational modification of Rab10 could be disease-relevant. Whether Rab10's phosphorylation status affects its ability to regulate prion-like activity of $mHTT_{ex1}$ or other amyloid aggregates warrants further investigation.

In conclusion, our findings demonstrate that axonal $mHTT_{ex1}$ aggregates activate glial phagocytosis but also impair normal glial responses to acute neural injury. Aggregate engulfment-induced defects in endolysosomal processing, such as Rab-mediated vesicle membrane fusion, could facilitate the formation and spread of prion-like aggregate seeds in the brain. These findings point to central roles for the glial endo/phagosomal system in regulating pathological aggregate burden in HD and highlight the importance of exploring therapeutic interventions that target non-neuronal cells.

References

Aits S, et al. (2015) Sensitive detection of lysosomal membrane permeabilization by lysosomal galectin puncta assay. Autophagy 11:1408–1424.
Aman Y, et al. (2021) Autophagy in healthy aging and disease. Nat Aging 1: 634–650.
Bae E-J, et al. (2018) LRRK2 kinase regulates α-synuclein propagation via RAB35 phosphorylation. Nat Commun 9:3465.
Bonam SR, Wang F, Muller S (2019) Lysosomes as a therapeutic target. Nat Rev Drug Discov 18:923–948.
Brand AH, Perrimon N (1993) Targeted gene expression as a means of altering cell fates and generating dominant phenotypes. Development 18:401–415.
Brelstaff JH, Mason M, Katsinelos T, McEwan WA, Ghetti B, Tolkovsky AM, Spillantini MG (2021) Microglia become hypofunctional and release metalloproteases and tau seeds when phagocytosing live neurons with P301S tau aggregates. Sci Adv 7:eabg4980.
Burbidge K, et al. (2022) LGALS3 (galectin 3) mediates an unconventional secretion of SNCA/α-synuclein in response to lysosomal membrane damage by the autophagic-lysosomal pathway in human midbrain dopamine neurons. Autophagy 18:1020–1048.
Byrns CN, Saikumar J, Bonini NM (2021) Glial AP1 is activated with aging and accelerated by traumatic brain injury. Nat Aging 1:585–597.
Cardoso CMP, Jordao L, Vieira OV (2010) Rab10 regulates phagosome maturation and its overexpression rescues mycobacterium-containing phagosomes maturation. Traffic 11:221–235.
Casula M, Iyer AM, Spliet WGM, Anink JJ, Steentjes K, Sta M, Troost D, Aronica E (2011) Toll-like receptor signaling in amyotrophic lateral sclerosis spinal cord tissue. Neuroscience 179:233–243.
Chan C-C, et al. (2011) Systematic discovery of Rab GTPases with synaptic functions in *Drosophila*. Curr Biol 21:1704–1715.
Chen JJ, et al. (2019) Compromised function of the ESCRT pathway promotes endolysosomal escape of tau seeds and propagation of tau aggregation. J Biol Chem 294:18952–18966.
Chen S, Berthelier V, Yang W, Wetzel R (2001) Polyglutamine aggregation behavior in vitro supports a recruitment mechanism of cytotoxicity. J Mol Biol 311:173–182.
Choi I, Zhang Y, Seegobin SP, Pruvost M, Wang Q, Purtell K, Zhang B, Yue Z (2020) Microglia clear neuron-released α-synuclein via selective autophagy and prevent neurodegeneration. Nat Commun 11:1386.
Chung W-S, et al. (2013) Astrocytes mediate synapse elimination through MEGF10 and MERTK pathways. Nature 504:394–400.
Couto A, Alenius M, Dickson BJ (2005) Molecular, anatomical, and functional organization of the *Drosophila* olfactory system. Curr Biol 15:1535–1547.
Daussy CF, Wodrich H (2020) "Repair me if you can": membrane damage, response, and control from the viral perspective. Cells 9:2042.
Dejanovic B, et al. (2022) Complement C1q-dependent excitatory and inhibitory synapse elimination by astrocytes and microglia in Alzheimer's disease mouse models. Nat Aging 2:837–850.
Doherty J, Logan MA, Taşdemir OE, Freeman MR (2009) Ensheathing glia function as phagocytes in the adult *Drosophila* brain. J Neurosci 29: 4768–4781.
Donnelly KM, Coleman CM, Fuller ML, Reed VL, Smerina D, Tomlinson DS, Pearce MMP (2022) Hunting for the cause: evidence for prion-like mechanisms in Huntington's disease. Front Neurosci 16:946822.

Donnelly KM, DeLorenzo OR, Zaya AD, Pisano GE, Thu WM, Luo L, Kopito RR, Panning Pearce MM (2020) Phagocytic glia are obligatory intermediates in transmission of mutant huntingtin aggregates across neuronal synapses. Elife 9:e58499.
Dunlop J, Jones PC, Finbow ME (1995) Membrane insertion and assembly of ductin: a polytopic channel with dual orientations. EMBO J 14:3609–3616.
Dunst S, et al. (2015) Endogenously tagged Rab proteins: a resource to study membrane trafficking in *Drosophila*. Dev Cell 33:351–365.
Duong L, Radley H, Lee B, Dye D, Pixley F, Grounds M, Nelson DJ, Jackaman C (2021) Macrophage function in the elderly and impact on injury repair and cancer. Immun Ageing 18:4.
Eapen VV, Swarup S, Hoyer MJ, Paulo JA, Harper JW (2021) Quantitative proteomics reveals the selectivity of ubiquitin-binding autophagy receptors in the turnover of damaged lysosomes by lysophagy. Elife 10: e72328.
Eguchi T, et al. (2018) LRRK2 and its substrate Rab GTPases are sequentially targeted onto stressed lysosomes and maintain their homeostasis. Proc Natl Acad Sci U S A 115:E9115–E9124.
Evans IR, Rodrigues FSLM, Armitage EL, Wood W (2015) Draper/CED-1 mediates an ancient damage response to control inflammatory blood cell migration in vivo. Curr Biol 25:1606–1612.
Falcon B, Noad J, McMahon H, Randow F, Goedert M (2018) Galectin-8–mediated selective autophagy protects against seeded tau aggregation. J Biol Chem 293:2438–2451.
Finbow ME, Goodwin SF, Meagher L, Lane NJ, Keen J, Findlay JBC, Kaiser K (1994) Evidence that the 16 kDa proteolipid (subunit c) of the vacuolar H +-ATPase and ductin from gap junctions are the same polypeptide in *Drosophila* and *Manduca*: molecular cloning of the Vha16k gene from *Drosophila*. J Cell Sci 107:1817–1824.
Flavin WP, Bousset L, Green ZC, Chu Y, Skarpathiotis S, Chaney MJ, Kordower JH, Melki R, Campbell EM (2017) Endocytic vesicle rupture is a conserved mechanism of cellular invasion by amyloid proteins. Acta Neuropathol 134:629–653.
Freeman D, et al. (2013) Alpha-synuclein induces lysosomal rupture and cathepsin dependent reactive oxygen species following endocytosis. PLoS One 8:e62143.
Fujita Y, et al. (2020) Engulfment of toxic amyloid β-protein in neurons and astrocytes mediated by MEGF10. Neuroscience 443:1–7.
Ginsberg SD, Mufson EJ, Alldred MJ, Counts SE, Wuu J, Nixon RA, Che S (2011) Upregulation of select rab GTPases in cholinergic basal forebrain neurons in mild cognitive impairment and Alzheimer's disease. J Chem Neuroanat 42:102–110.
Hall A (1990) The cellular functions of small GTP-binding proteins. Science 249:635–640.
Han C, Song Y, Xiao H, Wang D, Franc NC, Jan LY, Jan YN (2014) Epidermal cells are the primary phagocytes in the fragmentation and clearance of degenerating dendrites in *Drosophila*. Neuron 81:544–560.
Heckmann BL, Teubner BJW, Tummers B, Boada-Romero E, Harris L, Yang M, Guy CS, Zakharenko SS, Green DR DR (2019) LC3-associated endocytosis facilitates β-amyloid clearance and mitigates neurodegeneration in murine Alzheimer's disease. Cell 178:536.
Herzog C, Pons Garcia L, Keatinge M, Greenald D, Moritz C, Peri F, Herrgen L (2019) Rapid clearance of cellular debris by microglia limits secondary neuronal cell death after brain injury in vivo. Development 146: dev174698.
Homma Y, Hiragi S, Fukuda M (2021) Rab family of small GTPases: an updated view on their regulation and functions. FEBS J 288:36–55.
Hong S, et al. (2016) Complement and microglia mediate early synapse loss in Alzheimer mouse models. Science 352:712–716.
Hopp SC, Lin Y, Oakley D, Roe AD, DeVos SL, Hanlon D, Hyman BT (2018) The role of microglia in processing and spreading of bioactive tau seeds in Alzheimer's disease. J Neuroinflammation 15:269.
Hutagalung AH, Novick PJ (2011) Role of Rab GTPases in membrane traffic and cell physiology. Physiol Rev 91:119–149.
Iram T, Ramirez-Ortiz Z, Byrne MH, Coleman UA, Kingery ND, Means TK, Frenkel D, El Khoury J (2016) Megf10 is a receptor for C1Q that mediates clearance of apoptotic cells by astrocytes. J Neurosci 36:5185–5192.
Ito K, Urban J, Technau GM (1995) Distribution, classification, and development of Drosophila glial cells in the late embryonic and early larval ventral nerve cord. Rouxs Arch Dev Biol 204:284–307.
Jain N, Lewis CA, Ulrich JD, Holtzman DM (2023) Chronic TREM2 activation exacerbates Aβ-associated tau seeding and spreading. J Exp Med 220: e20220654.
Jeong GR, et al. (2018) Dysregulated phosphorylation of Rab GTPases by LRRK2 induces neurodegeneration. Mol Neurodegener 13:8.
Jia J, et al. (2020) Galectin-3 coordinates a cellular system for lysosomal repair and removal. Dev Cell 52:69–87.e8.
Jiang S, Bhaskar K (2020) Degradation and transmission of Tau by autophagic-endolysosomal networks and potential therapeutic targets for tauopathy. Front Mol Neurosci 13:586731.
Jiang P, Gan M, Yen S-H, McLean PJ, Dickson DW (2017) Impaired endolysosomal membrane integrity accelerates the seeding progression of α-synuclein aggregates. Sci Rep 7:7690.
Jucker M, Walker LC (2018) Propagation and spread of pathogenic protein assemblies in neurodegenerative diseases. Nat Neurosci 21:1341–1349.
Karran E, De Strooper B (2022) The amyloid hypothesis in Alzheimer disease: new insights from new therapeutics. Nat Rev Drug Discov 21:306–318.
Katzenberger RJ, Loewen CA, Wassarman DR, Petersen AJ, Ganetzky B, Wassarman DA (2013) A *Drosophila* model of closed head traumatic brain injury. Proc Natl Acad Sci U S A 110:E4152–E4159.
Kiral FR, Kohrs FE, Jin EJ, Hiesinger PR (2018) Rab GTPases and membrane trafficking in neurodegeneration. Curr Biol 28:R471–R486.
Kluss JH, Beilina A, Williamson CD, Lewis PA, Cookson MR, Bonet-Ponce L (2022) Lysosomal positioning regulates Rab10 phosphorylation at LRRK2 + lysosomes. Proc Natl Acad Sci U S A 119:e2205492119.
Knowles TPJ, Vendruscolo M, Dobson CM (2014) The amyloid state and its association with protein misfolding diseases. Nat Rev Mol Cell Biol 15: 384–396.
Kohrs FE, et al. (2021) Systematic functional analysis of rab GTPases reveals limits of neuronal robustness to environmental challenges in flies. Elife 10:e59594.
Koreman GT, Xu Y, Hu Q, Zhang Z, Allen SE, Wolfner MF, Wang B, Han C (2021) Upgraded CRISPR/Cas9 tolls for tissue-specific mutagenesis in Drosophila. Proc Natl Acad Sci U S A 118:e2014255118 .
Kouli A, Camacho M, Allinson K, Williams-Gray CH (2020) Neuroinflammation and protein pathology in Parkinson's disease dementia. Acta Neuropathol Commun 8:211.
Krasemann S, et al. (2017) The TREM2-APOE pathway drives the transcriptional phenotype of dysfunctional microglia in neurodegenerative diseases. Immunity 47:566–581.e9.
Langemeyer L, Fröhlich F, Ungermann C (2018) Rab GTPase function in endosome and lysosome biogenesis. Trends Cell Biol 28:957–970.
Larsson MC, Domingos AI, Jones WD, Chiappe ME, Amrein H, Vosshall LB (2004) Or83b encodes a broadly expressed odorant receptor essential for *Drosophila* olfaction. Neuron 43:703–714.
Lee H, et al. (2020) LRRK2 is recruited to phagosomes and co-recruits RAB8 and RAB10 in human pluripotent stem cell-derived macrophages. Stem Cell Rep 14:940–955.
Lee J-H, et al. (2022) Faulty autolysosome acidification in Alzheimer's disease mouse models induces autophagic build-up of Aβ in neurons, yielding senile plaques. Nat Neurosci 25:688–701.
Lee J-H, Kim J-Y, Noh S, Lee H, Lee SY, Mun JY, Park H, Chung WS (2021) Astrocytes phagocytose adult hippocampal synapses for circuit homeostasis. Nature 590:612–617.
Leyns CEG, et al. (2019) TREM2 function impedes tau seeding in neuritic plaques. Nat Neurosci 22:1217–1222.
Liang L, Li Y, Potter CJ, Yizhar O, Deisseroth K, Tsien RW, Luo L (2013) GABAergic projection neurons route selective olfactory inputs to specific higher order neurons. Neuron 79:917–931.
Liddelow SA, et al. (2017) Neurotoxic reactive astrocytes are induced by activated microglia. Nature 541:481–487.
Liddelow SA, Marsh SE, Stevens B (2020) Microglia and astrocytes in disease: dynamic duo or partners in crime? Trends Immunol 41:820–835.
Liu C-C, Hu J, Zhao N, Wang J, Wang N, Cirrito JR, Kanekiyo T, Holtzman DM, Bu G (2017) Astrocytic LRP1 mediates brain Aβ clearance and impacts amyloid deposition. J Neurosci 37:4023–4031.
Liu Z, Xu E, Zhao HT, Cole T, West AB (2020) LRRK2 and Rab10 coordinate macropinocytosis to mediate immunological responses in phagocytes. EMBO J 39:e104862.
Logan MA, Hackett R, Doherty J, Sheehan A, Speese SD, Freeman MR (2012) Negative regulation of glial engulfment activity by Draper terminates glial responses to axon injury. Nat Neurosci 15:722–730.
MacDonald JM, Beach MG, Porpiglia E, Sheehan AE, Watts RJ, Freeman MR (2006) The *Drosophila* cell corpse engulfment receptor Draper mediates glial clearance of severed axons. Neuron 50:869–881.
Magaki SD, Williams CK, Vinters HV (2018) Glial function (and dysfunction) in the normal & ischemic brain. Neuropharmacology 134:218–225.

Marischuk K, Crocker KL, Ahern-Djamali S, Boekhoff-Falk G (2021) Innate immunity pathways activate cell proliferation after penetrating traumatic brain injury in adult *Drosophila*. 2021.09.01.458615.
McGuire SE, Le PT, Davis RL (2001) The role of *Drosophila* mushroom body signaling in olfactory memory. Science 293:1330–1333.
McLaughlin CN, Perry-Richardson JJ, Coutinho-Budd JC, Broihier HT (2019) Dying neurons utilize innate immune signaling to prime glia for phagocytosis during development. Dev Cell 48:506–522.e6.
Miesenböck G, De Angelis DA, Rothman JE (1998) Visualizing secretion and synaptic transmission with pH-sensitive green fluorescent proteins. Nature 394:192–195.
Miron J, Picard C, Frappier J, Dea D, Théroux L, Poirier J (2018) TLR4 gene expression and pro-inflammatory cytokines in Alzheimer's disease and in response to hippocampal deafferentation in rodents. J Alzheimers Dis 63: 1547–1556.
Monaco A, Fraldi A (2020) Protein aggregation and dysfunction of autophagy–lysosomal pathway: a vicious cycle in lysosomal storage diseases. Front Mol Neurosci 13:37.
Neniskyte U, Neher JJ, Brown GC (2011) Neuronal death induced by nanomolar amyloid β is mediated by primary phagocytosis of neurons by microglia*. J Biol Chem 286:39904–39913.
Ng EL, Tang BL (2008) Rab GTPases and their roles in brain neurons and glia. Brain Res Rev 58:236–246.
Paolicelli RC, et al. (2011) Synaptic pruning by microglia is necessary for normal brain development. Science 333:1456–1458.
Parhizkar S, et al. (2019) Loss of TREM2 function increases amyloid seeding but reduces plaque-associated ApoE. Nat Neurosci 22:191–204.
Pearce MMP, Spartz EJ, Hong W, Luo L, Kopito RR (2015) Prion-like transmission of neuronal huntingtin aggregates to phagocytic glia in the *Drosophila* brain. Nat Commun 6:6768.
Podleśny-Drabiniok A, Marcora E, Goate AM (2020) Microglial phagocytosis: a disease-associated process emerging from Alzheimer's disease genetics. Trends Neurosci 43:965–979.
Poe AR, et al. (2019) Robust CRISPR/Cas9-mediated tissue-specific mutagenesis reveals gene redundancy and perdurance in *Drosophila*. Genetics 211: 459–472.
Polanco JC, Götz J (2022) Exosomal and vesicle-free tau seeds—propagation and convergence in endolysosomal permeabilization. FEBS J 289:6891–6907.
Portela M, Yang L, Paul S, Li X, Veraksa A, Parsons LM, Richardson HE (2018) Lgl reduces endosomal vesicle acidification and notch signaling by promoting the interaction between Vap33 and the V-ATPase complex. Sci Signal 11:eaar1976.
Potter CJ, Luo L (2011) Using the Q system in *Drosophila*. Nat Protoc 6:1105–1120.
Preisinger E, Jordan BM, Kazantsev A, Housman D (1999) Evidence for a recruitment and sequestration mechanism in Huntington's disease. Philos Trans R Soc Lond B Biol Sci 354:1029–1034.
Prince E, Kroeger B, Gligorov D, Wilson C, Eaton S, Karch F, Brankatschk M, Maeda RK (2019) Rab-mediated trafficking in the secondary cells of *Drosophila* male accessory glands and its role in fecundity. Traffic 20: 137–151.
Pulipparacharuvil S, Akbar MA, Ray S, Sevrioukov EA, Haberman AS, Rohrer J, Krämer H (2005) *Drosophila* Vps16A is required for trafficking to lysosomes and biogenesis of pigment granules. J Cell Sci 118:3663–3673.
Purice MD, Ray A, Münzel EJ, Pope BJ, Park DJ, Speese SD, Logan MA (2017) A novel *Drosophila* injury model reveals severed axons are cleared through a Draper/MMP-1 signaling cascade. Elife 6:e23611.
Purice MD, Speese SD, Logan MA (2016) Delayed glial clearance of degenerating axons in aged *Drosophila* is due to reduced PI3K/Draper activity. Nat Commun 7:12871.
Raiders S, Han T, Scott-Hewitt N, Kucenas S, Lew D, Logan MA, Singhvi A (2021) Engulfed by glia: glial pruning in development, function, and injury across species. J Neurosci 41:823–833.
Ray A, Speese SD, Logan MA (2017) Glial Draper rescues Aβ toxicity in a *Drosophila* model of Alzheimer's disease. J Neurosci 37:11881–11893.
Ridge PG, et al. (2017) Linkage, whole genome sequence, and biological data implicate variants in RAB10 in Alzheimer's disease resilience. Genome Med 9:100.
Rivero-Ríos P, Romo-Lozano M, Fernández B, Fdez E, Hilfiker S (2020) Distinct roles for RAB10 and RAB29 in pathogenic LRRK2-mediated endolysosomal trafficking alterations. Cells 9:1719.
Rodrigues PV, de Godoy JVP, Bosque BP, Amorim Neto DP, Tostes K, Palameta S, Garcia-Rosa S, Tonoli CCC, de Carvalho HF, de Castro Fonseca M (2022) Transcellular propagation of fibrillar α-synuclein from enteroendocrine to neuronal cells requires cell-to-cell contact and is Rab35-dependent. Sci Rep 12:4168.
Rodriguez L, Mohamed N-V, Desjardins A, Lippé R, Fon EA, Leclerc N (2017) Rab7a regulates tau secretion. J Neurochem 141:592–605.
Rong Y, McPhee CK, Deng S, Huang L, Chen L, Liu M, Tracy K, Baehrecke EH, Yu L, Lenardo MJ (2011) Spinster is required for autophagic lysosome reformation and mTOR reactivation following starvation. Proc Natl Acad Sci U S A 108:7826–7831.
Santra M, Dill KA, de Graff AMR (2019) Proteostasis collapse is a driver of cell aging and death. Proc Natl Acad Sci U S A 116:22173–22178.
Sapar ML, Ji H, Wang B, Poe AR, Dubey K, Ren X, Ni J-Q, Han C (2018) Phosphatidylserine externalization results from and causes neurite degeneration in Drosophila. Cell Rep 24:2273–2286.
Scherzinger E, Sittler A, Schweiger K, Heiser V, Lurz R, Hasenbank R, Bates GP, Lehrach H, Wanker EE (1999) Self-assembly of polyglutamine-containing huntingtin fragments into amyloid-like fibrils: implications for Huntington's disease pathology. Proc Natl Acad Sci U S A 96:4604–4609.
Seol W, Nam D, Son I (2019) Rab GTPases as physiological substrates of LRRK2 kinase. Exp Neurobiol 28:134–145.
Sepp KJ, Schulte J, Auld VJ (2001) Peripheral glia direct axon guidance across the CNS/PNS transition zone. Dev Biol 238:47–63.
Seto S, Tsujimura K, Koide Y (2011) Rab GTPases regulating phagosome maturation are differentially recruited to mycobacterial phagosomes. Traffic 12:407–420.
Singh TD, Park S-Y, Bae J, Yun Y, Bae Y-C, Park R-W, Kim IS (2010) MEGF10 functions as a receptor for the uptake of amyloid-β. FEBS Lett 584:3936–3942.
Small SA, Simoes-Spassov S, Mayeux R, Petsko GA (2017) Endosomal traffic jams represent a pathogenic hub and therapeutic target in Alzheimer's disease. Trends Neurosci 40:592–602.
Steger M, et al. (2016) Phosphoproteomics reveals that Parkinson's disease kinase LRRK2 regulates a subset of Rab GTPases. Elife 5:e12813.
Stein KC, Morales-Polanco F, van der Lienden J, Rainbolt TK, Frydman J (2022) Ageing exacerbates ribosome pausing to disrupt cotranslational proteostasis. Nature 601:637–642.
Streubel-Gallasch L, et al. (2021) Parkinson's disease–associated LRRK2 interferes with astrocyte-mediated alpha-synuclein clearance. Mol Neurobiol 58:3119–3140.
Swanson LC, Rimkus SA, Ganetzky B, Wassarman DA (2020a) Loss of the antimicrobial peptide metchnikowin protects against traumatic brain injury outcomes in *Drosophila melanogaster*. G3 10:3109–3119.
Swanson LC, Trujillo EA, Thiede GH, Katzenberger RJ, Shishkova E, Coon JJ, Ganetzky B, Wassarman DA (2020b) Survival following traumatic brain injury in *Drosophila* is increased by heterozygosity for a mutation of the NF-κB innate immune response transcription factor relish. Genetics 216: 1117–1136.
Tavana JP, Rosene M, Jensen NO, Ridge PG, Kauwe JS, Karch CM (2018) RAB10: an Alzheimer's disease resilience locus and potential drug target. Clin Interv Aging 14:73–79.
Tezuka T, et al. (2022) Pathophysiological evaluation of the LRRK2 G2385R risk variant for Parkinson's disease. NPJ Parkinsons Dis 8:97.
Udayar V, et al. (2013) A paired RNAi and RabGAP overexpression screen identifies Rab11 as a regulator of β-amyloid production. Cell Rep 5: 1536–1551.
Udayar V, Chen Y, Sidransky E, Jagasia R (2022) Lysosomal dysfunction in neurodegeneration: emerging concepts and methods. Trends Neurosci 45:184–199.
Ugbode C, Fort-Aznar L, Sweeney ST (2019) Leaky endosomes push tau over the seed limit. J Biol Chem 294:18967–18968.
van Alphen B, et al. (2022) Glial immune-related pathways mediate effects of closed head traumatic brain injury on behavior and lethality in *Drosophila*. PLoS Biol 20:e3001456.
Vieira OV, Botelho RJ, Grinstein S (2002) Phagosome maturation: aging gracefully. Biochem J 366:689–704.
Wakida NM, Cruz GMS, Ro CC, Moncada EG, Khatibzadeh N, Flanagan LA, Berns MW (2018) Phagocytic response of astrocytes to damaged neighboring cells. PLoS One 13:e0196153.
Wang C, et al. (2022) Microglial NF-κB drives tau spreading and toxicity in a mouse model of tauopathy. Nat Commun 13:1969.
Wang Y, et al. (2023) Large vesicle extrusions from C. elegans neurons are consumed and stimulated by glial-like phagocytosis activity of the neighboring cell. Elife 12:e82227.

Wanker EE (2000) Protein aggregation and pathogenesis of Huntingtons disease: mechanisms and correlations. Biol Chem 381:937–942.
Welikovitch LA, Dujardin S, Dunn AR, Fernandes AR, Khasnavis A, Chibnik LB, Kaczorowski CC, Hyman BT (2023) Rate of tau propagation is a heritable disease trait in genetically diverse mouse strains. iScience 26: 105983.
Wodrich APK, Scott AW, Shukla AK, Harris BT, Giniger E (2022) The unfolded protein responses in health, aging, and neurodegeneration: recent advances and future considerations. Front Mol Neurosci 15:831116.
Yan Y, Denef N, Schüpbach T (2009) The vacuolar proton pump (V-ATPase) is required for notch signaling and endosomal trafficking in *Drosophila*. Dev Cell 17:387–402.
Yan T, Wang L, Gao J, Siedlak SL, Huntley ML, Termsarasab P, Perry G, Chen SG, Wang X (2018) Rab10 phosphorylation is a prominent pathological feature in Alzheimer's disease. J Alzheimers Dis 63:157–165.
Yuste-Checa P, Trinkaus VA, Riera-Tur I, Imamoglu R, Schaller TF, Wang H, Dudanova I, Hipp MS, Bracher A, Hartl FU (2021) The extracellular chaperone Clusterin enhances tau aggregate seeding in a cellular model. Nat Commun 12:4863.
Zhang J, Schulze KL, Hiesinger PR, Suyama K, Wang S, Fish M, Acar M, Hoskins RA, Bellen HJ, Scott MP (2007) Thirty-one flavors of *Drosophila* Rab proteins. Genetics 176:1307–1322.
Zheng B, Tuszynski MH (2023) Regulation of axonal regeneration after mammalian spinal cord injury. Nat Rev Mol Cell Biol 24:396–413.